A spatial map of hepatic mitochondria uncovers functional heterogeneity shaped by nutrient-sensing signaling

Sun Woo Sophie Kang[1], Rory P. Cunningham[1], Colin B. Miller[1], Constance M. Cultraro[1], Jonathan Hernandez[2], Lisa M. Jenkins[3] , Alexei Lobanov[4], Maggie Cam[4], and Natalie Porat-Shliom[1,5]

1. Cell Biology and Imaging Section, Thoracic and GI Malignancies Branch, National Cancer Institute (NCI), National Institutes of Health (NIH), Bethesda, Maryland, USA.
2. Surgical Oncology Program, National Cancer Institute (NCI), National Institutes of Health (NIH), Bethesda, Maryland, USA.
3. Laboratory of Cell Biology, National Cancer Institute (NCI), National Institutes of Health (NIH), Bethesda, Maryland, USA.
4. CCR Collaborative Bioinformatics Resource (CCBR) National Cancer Institute (NCI), National Institutes of Health (NIH), Bethesda, Maryland, USA.
5. Correspondence: natalie.porat-shliom@nih.gov

Abstract

In the liver, mitochondria are exposed to different concentrations of nutrients due to their spatial positioning across the periportal (PP) and pericentral (PC) axis. How these mitochondria sense and integrate these signals to respond and maintain homeostasis is not known. Here, we combined intravital microscopy, spatial proteomics, and functional assessment to investigate mitochondrial heterogeneity in the context of liver zonation. We found that PP and PC mitochondria are morphologically and functionally distinct; beta-oxidation and mitophagy were elevated in PP regions, while lipid synthesis was predominant in the PC mitochondria. In addition, comparative phosphoproteomics revealed that mitophagy and lipid synthesis are regulated by phosphorylation in a zonated manner. Furthermore, we demonstrated that acute pharmacological modulation of nutrient sensing through AMPK and mTOR shifted mitochondrial phenotypes in the PP and PC regions of the intact liver. This study highlights the role of protein phosphorylation in mitochondrial structure, function, and overall homeostasis in hepatic metabolic zonation. The findings have important implications for liver physiology and disease.

Introduction

Mitochondria are highly dynamic organelles that play critical roles in cell physiology, including energy production through oxidative phosphorylation (OXPHOS), metabolic signaling pathways, and biosynthesis [1-5]. In response to changes in the environment, like nutrient availability, mitochondria undergo remodeling through fission, fusion, and mitophagy [2,4]. These dynamic rearrangements in mitochondrial architecture are fundamental to mitochondrial function, morphology and homeostasis [4,5]. Further, these dynamic changes are modulated, in part, through post-translational modifications, like phosphorylation, allowing mitochondria to rapidly and reversibly adjust their metabolic output [6-8]. *In vivo*, mitochondria in cells within organs are exposed to varying levels of nutrients due to their spatial positioning with respect to the blood supply. How this affects and/or regulates mitochondrial dynamics is not known.

This is particularly important in the liver, a central metabolic organ that balances whole-body nutrient availability. Within the liver, hepatocytes are organized into polygonal units called lobules. Nutrient-rich blood flows unidirectionally into the lobule, entering through the hepatic artery and portal vein (which will hence be referred to as periportal; PP) and drains into a single central vein (pericentral; PC). Consequently, the hepatocytes are exposed to different levels of regional metabolites and metabolic burdens depending on their relative location within the lobule [9,10]. It has been previously shown that these gradients cause hepatocytes in different parts of the lobule to express different genes, a phenomenon known as liver zonation [10]. Although single-cell technologies have enhanced our understanding of liver zonation [11,12], the functional consequences are often inferred solely from gene expression.

Electron microscopy studies have revealed notable differences in mitochondrial morphology between PP and PC hepatocytes [13-16]. These observations suggest that cells on the PP-PC axis, separated by up to 300 μm, possess mitochondria with distinct functions. However, it is not known how spatial separation affects mitochondria functions *in vivo*. Furthermore, whether mitochondria variations are determined developmentally (by a molecular gradient along the sinusoid) or metabolically (via dynamic nutrient gradients) requires elucidation.

In the present study, we aimed to define the relationship between mitochondrial function, structure, and spatial positioning in the hepatic lobule. We also sought to identify

mechanisms that regulate mitochondrial function during homeostasis. Our results highlight the role of protein phosphorylation and nutrient sensing signaling in fine-tuning zonated mitochondria functions in the hepatic lobule. This is the first description of mitochondrial zonation in the liver, encompassing structural and functional features that reveal distinct subpopulations of mitochondria within the liver lobule.

Results

A comparative mitochondrial proteome of spatially sorted hepatocytes

To investigate how the spatial positioning of cells in the liver affects mitochondrial functions, PP and PC hepatocytes were enriched from the livers of four ad-lib-fed mice using unique surface markers and fluorescence-activated cell sorting (FACS; Fig 1A-C and [17]). E-cadherin and CD73 antibodies were used to enrich PP and PC hepatocytes, respectively, and western blot validation was performed to confirm enrichment (Fig 1D).

Next, PP and PC hepatocytes were subjected to tandem mass tag (TMT)-based quantitative mass spectrometry for total proteome analysis. The goal was to gain insight into mitochondrial functions by establishing a quantitative map of mitochondrial protein abundance along the PP-PC axis. Principal component and hierarchical clustering analysis showed sample grouping based on their spatial origin (PP or PC) (Fig S1A-B). Of 5,014 proteins identified, 46% were zonated, meaning they had a biased expression toward PP or PC hepatocytes (Fig. S1C-D). Pathway analysis highlighted PP and PC-restricted processes as previously described for gene expression [12] (Fig S1E-F).

The list of quantified proteins was compared with the murine MitoCarta 3.0 database, which consists of 1,140 proteins. We identified 826 mitochondrial proteins, of which 415 were enriched in PP mitochondria and 113 in PC mitochondria (Fig 2A and B). To gain insight into the functions of PP and PC mitochondria, the top 20 unique proteins were selected, and their location and pathway within the mitochondria were discerned using MitoCarta 3.0 database (Fig 2C and D).

Proteins enriched in PP mitochondria were primarily localized to the inner membrane or the matrix and were involved in amino acid metabolism or OXPHOS. We, therefore, examined the spatial expression of selected OXPHOS proteins and found that PP mitochondria expressed

higher levels of nuclear and mitochondrial-encoded OXPHOS components (Fig. 2E). In contrast, proteins enriched in PC mitochondria localized to the outer and inner mitochondrial membranes and matrix. Additionally, they were involved in a wider range of mitochondrial pathways, including those regulating mitochondrial structure, dynamics, and contact with other organelles. Many PC proteins are involved in lipid metabolism, detoxification, and carbohydrate metabolism (Fig. 2D). Notably, citrate synthase, a tricarboxylic acid cycle (TCA cycle) enzyme, was highly expressed in the PC mitochondria. Citrate is a precursor for lipid synthesis. Consistently, STRING analysis suggested a functional link between PC mitochondrial proteins involved in pyruvate metabolism and phospholipid membrane biosynthesis and lipid synthesis occurring in the cytosol (Fig 2F).

Periportal mitochondria display enhanced bioenergetic capacity

We next performed a functional evaluation of the PP and PC mitochondria to determine their bioenergetic capacity. Intravital microscopy [18] was used to examine mitochondrial membrane potential in the intact liver of anesthetized mice. Mitochondria were labeled with MitoTracker green and TMRE, with the former labeling mitochondria matrix and the latter indicating membrane potential. TMRE labeled mitochondria in PP regions more intensely, indicating higher membrane potential (Fig 3A and B). We ruled out non-uniform labeling due to disrupted perfusion since MitoTracker green delivered to all parts of the lobule was successful. Spatially sorted hepatocytes were also labeled in suspension with JC1, a ratiometric fluorescent reporter of mitochondrial membrane potential. Consistent with the *in vivo* data, PP cells labeled in suspension had higher mitochondrial membrane potential than PC cells (Fig 3C and D). Together, these data show that PP mitochondria have a higher membrane potential that is not disrupted by spatial sorting, allowing the use of these cells for further physiological evaluation.

Subsequently, mitochondrial respiration and substrate preferences were evaluated using the Seahorse XF Analyzer to measure the oxygen consumption rate in spatially sorted hepatocytes. PP mitochondria consumed up to double the amount of oxygen compared to PC mitochondria (Fig 3E) and had higher maximal respiration (Fig 3F). Next, we evaluated substrate preference by measuring the rate of ATP production in the presence of inhibitors. We found that the capacity of PP mitochondria to produce ATP was significantly decreased by etomoxir, an

irreversible inhibitor of fatty acid oxidation, whereas, in PC mitochondria, UK 5099, an inhibitor of the mitochondrial pyruvate carrier that inhibits pyruvate-dependent oxygen consumption, negatively impacted ATP production (Fig 3G and H).

ATP levels in PP hepatocytes were significantly higher as measured by a luminescent ATP Detection Kit (Fig 3I). In PC hepatocytes, on the other hand, citrate synthase activity was higher (Fig 3J), and so were the triglyceride (TG) levels (Fig 3K). Consistently, lipid droplets (LDs) that store TGs were more abundant in PC regions of the lobule (Fig S2A). Indeed, high ATP levels inhibit citrate synthase activity [19,20], suggesting that the lower ATP levels in PC hepatocytes may permit citrate synthase activity that can be used in the cytosol for lipogenesis. Together, our data suggest that PC mitochondria support lipogenesis during cellular homeostasis.

Interestingly, a recent study showed that the mRNA expression of enzymes involved in fatty acid synthesis were periportally zonated in the murine liver [21]. Likewise, we found that mRNA and protein abundance of Fasn (fatty acid synthase), Acly (ATP citrate synthase), Acaca (ACC1, acetyl-CoA carboxylase), and Scd1 (Stearoyl CoA desaturase 1) displayed a PP bias or were unzonated. However, these observations are inconsistent with the functional evaluation of lipogenesis (Fig S2B and C). This implies that functional specialization cannot always be inferred from expression data alone.

Mitochondrial morphology and organization vary across the hepatic lobule

To understand the spatial organization of mitochondria in the hepatic lobule, we used confocal microscopy to visualize mitochondria in liver sections from mito-Dendra2 mice [22]. Consistent with previous observations [13-16], an apparent dichotomy in mitochondrial architecture was observed along the PP-PC axis, with short, round mitochondria in PP and tubulated mitochondria in PC hepatocytes (Fig 4A). The transition between these two phenotypes occurred in the mid-lobular area, with a limited number of cells containing both phenotypes within a single cell (Fig 4A).

We further characterized mitochondrial morphology at the single-cell level using confocal microscopy. Specifically, we acquired high-resolution z-stacks (Movie S1 and S2), segmented individual cells and their mitochondria, generated mitochondrial surfaces using Imaris, and measured mitochondrial parameters, including sphericity, count, and volume (Movie S3 and S4).

This approach revealed the distinct subcellular organization of the mitochondrial network in hepatocytes from different parts of the lobule (Fig 4B and C). The sphericity index significantly differed between PP and PC, with mean values of 0.79 and 0.66, respectively. The higher mean values in PP hepatocytes indicate shape closer to a perfect circle (Fig 4D). Fewer mitochondrial counts were measured in PC hepatocytes (Fig 4E), consistent with lower mitochondria DNA copy number (Fig 4F). However, mitochondria in PC cells possessed a higher mitochondrial matrix volume (Fig 4G).

Interestingly, PP hepatocytes were consistently smaller than PC cells (compare Fig 4B and C). When the total mitochondrial volume was normalized to the cell size, there was no significant difference between PP and PC mitochondria, suggesting that the mitochondrial shape is functionally important. Because of the high mitochondrial content, we could not directly measure their surface area using confocal microscopy. We, therefore, indirectly evaluated surface area based on expression levels of outer and inner mitochondrial membrane proteins. Indeed, higher levels of outer membrane proteins Vdac1-3 (Fig 4H) and inner membrane Cox1 (Fig 2E) were expressed in PP mitochondria. Together, PP mitochondria may have a higher surface area-to-volume ratio, which is advantageous for OXPHOS. On the other hand, PC hepatocytes displayed a larger matrix volume when measured with MitoTracker green, which is consistent with processes such as lipid synthesis that are less dependent on the rate of oxygen diffusion (Fig 4G and I). Mitochondrial structural diversity, including the typical PP and PC morphologies described above, was conserved in the human liver, suggesting a similar structure-function relationship may apply (Fig S3). Taken together, mitochondrial structural variations across the lobule strongly correlate with the functional diversity in lipid oxidation and biosynthesis under normal physiological conditions.

Periportal mitochondria exhibit enhanced mitophagy

Mitophagy, the selective degradation of mitochondria via autophagy, is stimulated in response to various signals, including hypoxia, nutrient deprivation, and glucagon signaling [23,24]. Recently, it was shown that mitophagy is activated in response to OXPHOS stimulation [25]. In the liver, basal mitophagy is activated by the daily feeding and fasting cycle [26,27]. To evaluate if mitophagy was differentially regulated in the intact liver, we applied intravital microscopy of

mitochondria-targeted Keima of ad-lib-fed mice (mtKeima) [28]. The mtKeima protein has different excitation wavelengths depending on the acidity of the mitochondrial environment; in a neutral environment, mtKeima exhibits excitation at 440 nm, while in an acidic environment, excitation is at 560 nm (Fig 5A). The ratio of acidic-to-neutral excitation is a measure of mitophagy. We acquired tile scans of whole lobules and calculated ratios in regions of interest. Mitophagy was consistently higher in PP than in PC regions (Fig 5A and B). As expected, the protease inhibitor leupeptin led to the accumulation of mitochondria in lysosomes, blocking degradation (Fig S4A) and increasing the signal across the lobule (Fig 5B). Similar results were obtained with another mitophagy reporter Cox8-EGFP-mCherry [29] (Fig S4B and C). These results were surprising because previous studies have reported that mitophagy-related genes are expressed in PC cells suggesting that mitophagy is higher pericentrally [30,31]. Interestingly, we also observed the PC expression bias at the protein level (Fig 5C). Thus, basal mitophagy is higher in the metabolically active PP hepatocytes, which may maintain the levels of the mitophagy-related proteins low. This highlights that mitophagy cannot be predicted entirely from the expression levels of marker genes.

Phosphoproteome highlights spatially regulated pathways contributing to mitochondrial diversity

Reversible protein phosphorylation was linked to cellular and mitochondrial metabolism [6-8,32,33]. To examine the role of phosphorylation in regulating mitochondrial spatial heterogeneity and identify signaling pathways that may be involved, we determined the phosphoproteome profiles of PP and PC hepatocytes. We identified 7,278 phosphopeptides corresponding to 3686 phosphosites in 1,623 proteins (Fig 6A). The majority of phosphorylation sites were on serine residues (89%), with a smaller proportion identified on threonine (10%) and tyrosine (1%) (Fig 6B). More than half of the proteins had a single phosphorylation site (Fig 6C). Interestingly, the overall number of phosphosites with PP or PC zonation was similar (Fig 6D), suggesting that ATP availability across the lobule is not limiting in homeostasis.

Next, we performed a pathway analysis on phospho-peptides displaying zonal distribution to determine the processes that may be influenced by phosphorylation in each hepatocyte population. In PP hepatocytes, protein translation, metabolism, and positive regulation of

autophagy were most notably regulated via phosphorylation (Fig 6E). On the other hand, multiple pathways related to lipid and phospholipid synthesis were observed in PC cells (Fig 6F).

We also inspected the phosphorylation on mitochondrial proteins, with mitochondrial phosphoproteome shown in the volcano plot (Fig 6G) and the phosphoproteins that showed the strongest zonation for each hepatocyte group summarized in the table (Fig 6H). Interestingly, the mitochondrial fission proteins, Mtfr1 and Mtfr1l and mitophagy-related proteins, BNIP3 and Bcl2l13 were phosphorylated in PP hepatocytes, while pyruvate and lipid metabolism-related proteins such as Miga2 were identified as phosphorylated in PC hepatocytes. These results correlated with the higher mitophagy levels measured in PP hepatocytes (Fig 5A and B) and lipogenesis (Fig 3J-K and S2A), suggesting potential zonal regulation by phosphorylation and may explain the discordance between protein expression and function seen for mitophagy and lipogenesis.

Nutrient sensing signaling contributes to mitochondrial functional and structural heterogeneity across the lobule

Our findings suggest that mitophagy and lipogenesis may be regulated in a zonated manner via phosphorylation. These processes are also sensitive to nutrient availability and regulated by nutrient-sensitive kinases AMPK and mTOR [34,35]. Therefore, we hypothesized that nutrient-sensing signaling in hepatocytes governs mitochondrial remodeling in response to changes in nutrient availability. To test this, we pharmacologically modulated AMPK or mTOR signaling *in vivo* and evaluated mitochondrial membrane potential (JC1), volume (MitoTracker green), and lipid content (BODIPY) via flow cytometry in spatially sorted hepatocytes (Fig 7A-C). Drug concentrations for acute response were determined by western blotting of known downstream effectors (Fig S6A and B). Activation of AMPK (AICAR) and the inhibition of mTOR (Torin) were each associated with increased mitochondrial membrane potential in both PP and PC hepatocytes (Fig 7A). In PC cells, this was accompanied by a reduction in mitochondrial volume, making PC and PP mitochondrial volumes comparable (Fig 7B). Whereas mTOR inhibition reduced lipid content, AMPK activation had no effect (Fig 7C). This supports the idea that lower mitochondrial volume, typical of PP hepatocytes, may occur in conditions of AMPK activation or mTOR inhibition and in parallel with increased mitochondrial membrane potential.

The inhibition of AMPK (Compound C; Cpc), on the other hand, did not significantly impact mitochondrial membrane potential or mitochondria volume. It did, however, significantly increase lipid content in PC cells implying that AMPK may fulfill a role in regulating lipogenesis in PC as well (Fig 7C). Mitochondrial membrane potential was reduced, although not significantly, in response to mTOR activation (MHY1485) in PP or PC hepatocytes (Fig 7A). This also led to an increase in PC and PP mitochondrial volume and was accompanied by lipid accumulation, particularly in PP hepatocytes (Fig 7C). This supports the idea that large mitochondrial volume, typical of PC hepatocytes, occurs in conditions of mTOR activation and in parallel to increased lipid synthesis. Notably, the drugs had an acute effect on the mitochondria independent of cell size (Fig S6C). Overall, these experiments show that acute modulation of nutrient-sensing pathways shifts mitochondrial functions to impact mitochondrial functional diversity.

Finally, we performed microscopy studies in liver sections to examine if acute modulation of AMPK or mTOR induced mitochondrial morphology changes. PC mitochondria from AICAR-treated mice had a round, small morphology with a higher sphericity index, similar to PP mitochondria in vehicle-treated cells (Fig 7D and E). Conversely, mTOR activation induced dense, elongated mitochondria in PP hepatocytes, with a lower sphericity index resembling the phenotypes observed in PC hepatocytes (Fig 7D and E). These results demonstrate that AMPK activation shifted mitochondria morphology to a PP-like phenotype, while mTOR activation led to a PC-like morphology. Taken together, the results show that mitochondrial zonation is acutely remodeled *in vivo* by nutrient-sensing signaling suggesting the nutrient gradient along the sinusoid is sensed by hepatocytes to fine-tune the mitochondrial metabolic output.

Discussion

In this study, we performed an in-depth characterization of mouse hepatic mitochondria along the PP-PC axis. We assessed the spatial heterogeneity of these mitochondria in two populations of cells (Fig 1). We showed that mitochondria residing in hepatocytes adjacent to the portal vein produce significantly higher levels of ATP through lipid oxidation and OXPHOS and are turned over at a higher rate via mitophagy. Roughly 300 μm apart, PC mitochondria oxidize pyruvate and produce higher citrate levels for lipogenesis. This PP-PC dichotomy in mitochondrial

function mirrors the spatial separation of lipid utilization and biosynthesis in the liver. To our knowledge, this is the first spatial assessment of the molecular makeup and functional specialization of hepatic mitochondria. It is also the first in-depth investigation of how the physiological niche within the liver lobule alters mitochondrial metabolism. This location-dependent functional heterogeneity highlights the importance of considering mitochondrial disparity in understanding liver physiology and disease.

Consistent with previous observations [13-16], we also found striking variations in mitochondria morphology across the PP-PC axis (Fig 4). Specifically, small, spherical mitochondria correlated with enhanced OXPHOS in PP hepatocytes (Fig 2E and 4H). This morphology was previously shown to improve oxygen and nutrient exchange and tightly control calcium concentrations, an essential regulator of OXPHOS and mitophagy [25,36]. Conversely, longer, tubulated mitochondria (Fig 4C-D) entail a greater matrix volume (Fig 4G and 4I) which may promote enzymatic activities in the mitochondrial matrix, as observed in the case of citrate synthase in PC mitochondria (Fig 2D and 3J). Shirihai and colleagues recently demonstrated that mitochondrial fragmentation, such as we observe in PP hepatocytes, increases fatty acid oxidation [37]. We further demonstrated a correlation between hepatic mitochondrial structure and function; pharmacological modulation of AMPK and mTOR signaling pathways resulted in a remodeled mitochondrial structure and its corresponding function (Fig 7).

Tubular mitochondria were also shown to be protected from mitophagy [36], which further supports the observation of lower mitophagy levels in PC hepatocytes. Variations in mitochondrial fission and fusion are also likely to contribute to structural diversity, as has been previously shown in other tissues [38,39]. Indeed in PC mitochondria, we identified several candidates that may be involved in fusion pathways by regulating mitochondrial dynamics and contact sites (Fig 2D). On the other hand, mitochondrial morphology in PP hepatocytes suggests that fission is favored, which can be mediated by the phosphorylation of Mtfr1 or Mtfr1l (Fig 6H). Indeed, it was recently shown that AMPK phosphorylates Mtfr1l, which in turn leads to mitochondrial fragmentation [40]. Further experiments are necessary to examine the spatiotemporal regulation of mitochondrial fission-fusion dynamics as well as the examination of mitochondrial topology using higher-resolution imaging approaches. Our finding that

mitochondrial morphology is conserved in the human liver (Fig S3), suggests that some mechanisms are preserved across species and warrant further investigation.

In addition to displaying structural and functional heterogeneity, our study also revealed that a distinct mitochondrial phosphoproteome is associated with each mitochondrial population. This suggests unique cytosolic or mitochondrial kinases or phosphatases are active in different cells. Indeed, we identified spatially distinct kinases reported to regulate the mitochondrial phosphoproteome [6], including PKA (Prakaca) in PP mitochondria and, Pdha1 and Bckdc, in PC mitochondria (Fig 6H). Post-translational control of mitochondrial metabolism through phosphorylation has been shown to be critical across mouse strains, age, fasting/refeeding, and the onset of Type 2 diabetes [32]. Our study adds to this complexity by demonstrating that differential regulation observed across the lobule is fundamental to hepatic cellular homeostasis. While these phosphorylation sites were not characterized in this study, combining the phosphoproteome data with functional studies allowed us to gain a system-level perspective into the functional consequences of protein phosphorylation (Fig 6).

Our study also suggests that phosphorylation, rather than protein or gene expression, regulates mitochondrial quality control and lipid handling in a zonated manner. We were surprised by the inconsistency between the gene/protein expression of mitophagy-related genes (Fig 5C), lipogenesis enzymes (S2B-C), and the functional measurements *in vivo* (Fig 5A-B and Fig 3J-K). Multiple mitophagy-related proteins were phosphorylated in PP cells (Fig 6E,G, and H). Together with the measurements of mitophagy in tissues, these data support the idea that mitophagy is positively regulated via phosphorylation rather than protein abundance. Indeed, phosphorylation of BNIP3 was shown to promote mitophagy [41-43], including through phosphorylation of residues identified in this study (Fig 6H). Similarly, proteins related to lipid synthesis were abundantly phosphorylated in PC hepatocytes (Fig 6F-H). Therefore correlating the functional assays with pathway analysis of the phosphoproteome provided a unique perspective that phosphorylation may promote mitophagy in PP hepatocytes (Fig 6E) and lipid synthesis in PC hepatocytes (Fig 6F).

The regulation of mitophagy and lipogenesis through reversible phosphorylation is ideal. It can be remodeled by nutrient-sensitive kinases (Fig 7), thus providing a quick mechanism for

mitochondria to adjust their metabolic output. This is especially critical in the liver, given its role in maintaining whole-body glucose homeostasis. We speculate that post-translational modifications provide the flexibility required for these vital metabolic adjustments, compared to the relatively longer process of gene expression. Although further experiments to test this hypothesis are needed, we predict that protein phosphorylation may be the critical link between the observed discrepancies in function versus protein or gene expression. This finding has significant implications beyond the liver for studies where the function is inferred from expression.

Advances in omics approaches and microscopy technologies have opened up new avenues for research and discoveries in hepatic cell biology. Although liver zonation was described nearly a century ago, we are only now starting to unravel how liver anatomy and the gradient of factors within it affect liver function at the tissue level. For the first time, our study demonstrates the delicate interplay between the function, shape, and space of hepatic mitochondria. We show that an additional regulatory layer at the post-translational level exists, offering spatial and temporal control of hepatic activities. Other post-translational modifications are also likely at play. In the current study, due to the sample size required for phosphoproteome and functional assays, we were limited to analyzing only two groups of hepatocytes. Therefore, significant technological improvements are required to allow for further and deeper exploration of liver zonation. Such advances are already underway with single-cell proteomics [44], allowing increased spatial resolution in murine models and human samples. Ultimately, understanding how the local physiological niche affects mitochondrial metabolism may be relevant for the therapeutic modulation of these pathways in liver-related pathologies.

Contact information

Natalie Porat-Shliom, Center for Cancer Research, National Cancer Institute. Building 10, Room 12C207 MSC 1919, Bethesda, MD 20892. Phone: 240-760-6847. Email: natalie.porat-shliom@nih.gov

Financial Support

This work was supported by the Intramural Research Program at the NIH, National Cancer Institute (1ZIABC011828). The authors have no conflicts to report.

Acknowledgments

We thank Dr. Wen-Xing Ding for the Cox8-EGFP-mCherry-AAV8 construct. Mt-Keima mice were a gift from Drs. Torn Finkel and Nuo Sun. We thank Drs. Sudipto Das and Thorkell Andresson from the CCR proteomics Facility at the Frederick National Laboratory for Cancer Research. Dr. Daniel Feliciano acquired images in Figures 4A and S2A. We thank Pranali Pathare Mangat of 3P Scientific Communications for providing scientific editing support. We are grateful for the critical comments made by members of the Porat-Shliom lab.

References

1 Picard, M. & Shirihai, O. S. Mitochondrial signal transduction. *Cell Metab* **34**, 1620-1653 (2022). https://doi.org:10.1016/j.cmet.2022.10.008

2 Glancy, B. Visualizing Mitochondrial Form and Function within the Cell. *Trends Mol Med* **26**, 58-70 (2020). https://doi.org:10.1016/j.molmed.2019.09.009

3 Hoppins, S. The regulation of mitochondrial dynamics. *Curr Opin Cell Biol* **29**, 46-52 (2014). https://doi.org:10.1016/j.ceb.2014.03.005

4 Friedman, J. R. & Nunnari, J. Mitochondrial form and function. *Nature* **505**, 335-343 (2014). https://doi.org:10.1038/nature12985

5 Westermann, B. Bioenergetic role of mitochondrial fusion and fission. *Biochim Biophys Acta* **1817**, 1833-1838 (2012). https://doi.org:10.1016/j.bbabio.2012.02.033

6 Niemi, N. M. & Pagliarini, D. J. The extensive and functionally uncharacterized mitochondrial phosphoproteome. *Journal of Biological Chemistry* **297** (2021). https://doi.org:ARTN 100880 10.1016/j.jbc.2021.100880

7 Kolitsida, P. *et al.* Phosphorylation of mitochondrial matrix proteins regulates their selective mitophagic degradation (vol 116, pg 20517, 2019). *P Natl Acad Sci USA* **116**, 24374-24374 (2019). https://doi.org:10.1073/pnas.1918594116

8 Grimsrud, P. A. *et al.* A quantitative map of the liver mitochondrial phosphoproteome reveals posttranslational control of ketogenesis. *Cell Metab* **16**, 672-683 (2012). https://doi.org:10.1016/j.cmet.2012.10.004

9 Jungermann, K. in *Regulation of Hepatic Metabolism: Intra- and Intercellular Compartmentation* (eds Ronald G. Thurman, Frederick C. Kauffman, & Kurt Jungermann) 445-469 (Springer US, 1986).

10 Cunningham RP, P.-S. N. Liver Zonation – Revisiting Old Questions With New Technologies. *Front. Physiol.* (2021). https://doi.org:10.3389

11 Brosch, M. *et al.* Epigenomic map of human liver reveals principles of zonated morphogenic and metabolic control. *Nat Commun* **9**, 4150 (2018). https://doi.org:10.1038/s41467-018-06611-5
12 Halpern, K. B. *et al.* Single-cell spatial reconstruction reveals global division of labour in the mammalian liver. *Nature* **542**, 352-356 (2017). https://doi.org:10.1038/nature21065
13 Novikoff, A. B. Cell heterogeneity within the hepatic lobule of the rat: staining reactions. *J Histochem Cytochem* **7**, 240-244 (1959). https://doi.org:10.1177/7.4.240
14 Deane, H. W. A cytological study of the diurnal cycle of the liver of the mouse in relation to storage and secretion. *Anat Rec* **88**, 39-65 (1944). https://doi.org:DOI 10.1002/ar.1090880104
15 JM, K. Comparative and experimental studies on the cytology of the liver. (1933).
16 Smith, D. M. THE ONTOGENETIC HISTORY OF THE MITO- CHONDRIA OF THE HEPATIC CELL OF THE WHITE RAT. (1931).
17 Ben-Moshe, S. *et al.* Spatial sorting enables comprehensive characterization of liver zonation. *Nat Metab* **1**, 899-911 (2019). https://doi.org:10.1038/s42255-019-0109-9
18 Weigert, R., Porat-Shliom, N. & Amornphimoltham, P. Imaging cell biology in live animals: ready for prime time. *J Cell Biol* **201**, 969-979 (2013). https://doi.org:10.1083/jcb.201212130
19 Fang, M. & Lowenstein, J. M. Citrate and the conversion of carbohydrate into fat. The regulation of fatty acid synthesis by rat liver extracts. *Biochem J* **105**, 803-811 (1967). https://doi.org:10.1042/bj1050803
20 Shepherd, D. & Garland, P. B. The kinetic properties of citrate synthase from rat liver mitochondria. *Biochem J* **114**, 597-610 (1969). https://doi.org:10.1042/bj1140597
21 Massalha, H. *et al.* A single cell atlas of the human liver tumor microenvironment. *Mol Syst Biol* **16** (2020). https://doi.org:ARTN e9682 10.15252/msb.20209682
22 Pham, A. H., McCaffery, J. M. & Chan, D. C. Mouse lines with photo-activatable mitochondria to study mitochondrial dynamics. *Genesis* **50**, 833-843 (2012). https://doi.org:10.1002/dvg.22050
23 Macleod, K. F. Mitophagy and Mitochondrial Dysfunction in Cancer. *Annu Rev Canc Biol* **4**, 41-60 (2020). https://doi.org:10.1146/annurev-cancerbio-030419-033405
24 Palikaras, K., Lionaki, E. & Tavernarakis, N. Mechanisms of mitophagy in cellular homeostasis, physiology and pathology. *Nat Cell Biol* **20**, 1013-1022 (2018). https://doi.org:10.1038/s41556-018-0176-2
25 Han, S., Zhang, M., Jeong, Y. Y., Margolis, D. J. & Cai, Q. The role of mitophagy in the regulation of mitochondrial energetic status in neurons. *Autophagy* **17**, 4182-4201 (2021). https://doi.org:10.1080/15548627.2021.1907167
26 Manella, G. & Asher, G. The Circadian Nature of Mitochondrial Biology. *Front Endocrinol (Lausanne)* **7**, 162 (2016). https://doi.org:10.3389/fendo.2016.00162
27 Jacobi, D. *et al.* Hepatic Bmal1 Regulates Rhythmic Mitochondrial Dynamics and Promotes Metabolic Fitness. *Cell Metab* **22**, 709-720 (2015). https://doi.org:10.1016/j.cmet.2015.08.006
28 Sun, N. *et al.* Measuring In Vivo Mitophagy. *Mol Cell* **60**, 685-696 (2015). https://doi.org:10.1016/j.molcel.2015.10.009

29 Ma, X. & Ding, W. X. A fluorescence imaging based-assay to monitor mitophagy in cultured hepatocytes and mouse liver. *Liver Res* **5**, 16-20 (2021). https://doi.org:10.1016/j.livres.2020.12.002
30 Droin, C. *et al.* Space-time logic of liver gene expression at sub-lobular scale. *Nat Metab* (2021). https://doi.org:10.1038/s42255-020-00323-1
31 Springer, M. Z. *et al.* BNIP3-dependent mitophagy promotes cytosolic localization of LC3B and metabolic homeostasis in the liver. *Autophagy* **17**, 3530-3546 (2021). https://doi.org:10.1080/15548627.2021.1877469
32 Niemi, N. M. *et al.* Pptc7 is an essential phosphatase for promoting mammalian mitochondrial metabolism and biogenesis. *Nature Communications* **10** (2019). https://doi.org:ARTN 3197
10.1038/s41467-019-11047-6
33 Ardito, F., Giuliani, M., Perrone, D., Troiano, G. & Lo Muzio, L. The crucial role of protein phosphorylation in cell signaling and its use as targeted therapy. *International Journal of Molecular Medicine* **40**, 271-280 (2017). https://doi.org:10.3892/ijmm.2017.3036
34 Gonzalez, A., Hall, M. N., Lin, S. C. & Hardie, D. G. AMPK and TOR: The Yin and Yang of Cellular Nutrient Sensing and Growth Control. *Cell Metab* **31**, 472-492 (2020). https://doi.org:10.1016/j.cmet.2020.01.015
35 Herzig, S. & Shaw, R. J. AMPK: guardian of metabolism and mitochondrial homeostasis. *Nat Rev Mol Cell Biol* **19**, 121-135 (2018). https://doi.org:10.1038/nrm.2017.95
36 Rambold, A. S., Kostelecky, B., Elia, N. & Lippincott-Schwartz, J. Tubular network formation protects mitochondria from autophagosomal degradation during nutrient starvation. *Proceedings of the National Academy of Sciences* **108**, 10190-10195 (2011). https://doi.org:doi:10.1073/pnas.1107402108
37 Ngo, J. *et al.* Mitochondrial morphology controls fatty acid utilization by changing CPT1 sensitivity to malonyl-CoA. *Embo J*, e111901 (2023). https://doi.org:10.15252/embj.2022111901
38 Benador, I. Y. *et al.* Mitochondria Bound to Lipid Droplets Have Unique Bioenergetics, Composition, and Dynamics that Support Lipid Droplet Expansion. *Cell Metabolism* **27**, 869-+ (2018). https://doi.org:10.1016/j.cmet.2018.03.003
39 Porat-Shliom, N., Harding, O. J., Malec, L., Narayan, K. & Weigert, R. Mitochondrial Populations Exhibit Differential Dynamic Responses to Increased Energy Demand during Exocytosis In Vivo. *iScience* **11**, 440-449 (2019). https://doi.org:10.1016/j.isci.2018.12.036
40 Tilokani, L. *et al.* AMPK-dependent phosphorylation of MTFR1L regulates mitochondrial morphology. *Sci Adv* **8**, eabo7956 (2022). https://doi.org:10.1126/sciadv.abo7956
41 He, Y. L. *et al.* BNIP3 phosphorylation by JNK1/2 promotes mitophagy via enhancing its stability under hypoxia. *Cell Death Dis* **13**, 966 (2022). https://doi.org:10.1038/s41419-022-05418-z
42 Poole, L. P., Bock-Hughes, A., Berardi, D. E. & Macleod, K. F. ULK1 promotes mitophagy via phosphorylation and stabilization of BNIP3. *Sci Rep* **11**, 20526 (2021). https://doi.org:10.1038/s41598-021-00170-4
43 Cho, Y. K. *et al.* STK3/STK4 signalling in adipocytes regulates mitophagy and energy expenditure. *Nat Metab* **3**, 428-441 (2021). https://doi.org:10.1038/s42255-021-00362-2

44 Rosenberger, F. A. *et al.* Spatial single-cell mass spectrometry defines zonation of the hepatocyte proteome. *bioRxiv*, 2022.2012.2003.518957 (2022). https://doi.org:10.1101/2022.12.03.518957

Figure Legends

Figure 1. Spatial enrichment of PP and PC hepatocytes. (A) Schematic diagram depicting the workflow. Hepatocytes were isolated from the murine liver using two-step collagenase perfusion, after which unique surface markers were applied to label cells. Labeled cells were then enriched using fluorescence-activated cell sorting (FACS) to obtain hepatocytes from different zones. **(B)** Immunofluorescence staining of a liver section showing the zonal distribution of CD73 (cyan) and E-cadherin (magenta). **(C)** Two-dimensional scatter plot of hepatocytes labeled with CD73 and E-cadherin. **(D)** Western blot of spatially sorted hepatocytes.

Figure 2. Comparative mitochondrial proteome of spatially sorted hepatocytes. (A) The total number of non-mitochondrial proteins (grey) and mitochondrial proteins (green) was detected by mass spectrometry (left). Percentage of periportal (PP), pericentral (PC), and unzonated (UZ) mitochondrial proteins (right); expression based on a p-value (0.05). **(B)** Volcano plot shows the $\log_2$ PC/PP fold-change (x-axis) and the $-\log_{10}$ p-value (y-axis) for mitochondrial proteins. **(C-D)** Spatial distribution of the top 25 PP or PC mitochondrial proteins. Proteins were color-coded to reflect their cellular function. Pathways were listed based on the frequency at which they appeared. **(E)** The abundance of representative mitochondrial respiratory chain proteins, both nuclear and mitochondria encoded, are shown with box and whisker plots. **(F)** Bioinformatic STRING analysis of the PC mitochondria proteomic data. The interaction map illustrates the functional association of PC mitochondrial metabolism with cytosolic lipid synthesis. Data presented as mean ± SD. *$p < 0.05$, **$p < 0.01$, ***$p < 0.001$, ****$p < 0.0001$.

Figure S1. Comparative proteomics of spatially sorted hepatocytes. (A) Principal component analysis (PCA) and frequency histogram of spatially sorted hepatocytes analyzed with mass

spectrometry. **(B)** Correlation Matrix Heatmap of proteomics data. **(C)** Pie chart depicting the percentage of PP, PC, and UZ proteins based on p-value (0.05). **(D)** Volcano plot showing the *PC* to PP $\log_2$ fold-change (x-axis) and the $-\log_{10}$ p-value (y-axis) for identified proteins. **(E and F)** GO enrichment analysis of the proteomics data in the spatially sorted cell.

Figure 3. PP mitochondria display higher bioenergetic capacity. (A) Intravital microscopy of the hepatic lobule labeled with tetramethylrhodamine ethyl ester (TMRE), and MitoTracker Green to evaluate the relative mitochondrial membrane potential. The scale bar is 100 μm. **(B)** Mitochondrial membrane potential was evaluated by measuring fluorescence intensity (AU) along a PP-PC axis line. **(C-D)** Measurement of mitochondrial membrane potential using JC-1 and flow cytometry in spatially sorted hepatocytes. A representative experiment is shown in the dot plots. The bar graph shows three independent experiments. **(E)** Oxygen consumption rate (OCR) in spatially sorted hepatocytes using the XF Mito Stress Test Kit and Seahorse XF96 Analyzer. Samples were normalized to cell number. **(F)** Maximum respiration capacity in spatially sorted hepatocytes expressed relative to PP. The bar graph shows four independent experiments. **(G-H)** Substrate dependency assay in spatially sorted hepatocytes using the MitoFuel Flex test. ATP production rate relative to PP is shown in cells treated with either etomoxir, UK5099, or BPTES. The bar graph shows four independent experiments. **(I)** ATP content relative to PP in spatially sorted hepatocytes using the colorimetric luciferase assay from 3 independent experiments. **(J)** Citrate synthase activity relative to PP in spatially sorted hepatocytes from 5 independent experiments. **(K)** Intracellular triglyceride (TG) concentration relative to PP in spatially sorted hepatocytes from 3 independent experiments. Data presented as mean ± SD; ns, *$p < 0.05$, **$p < 0.01$, ***$p < 0.001$.

Figure S2. Lipid synthesis is pericentral in the murine liver. (A) Confocal image of the murine liver section labeled with Lipidtox (lipid droplets; red) and phalloidin (actin; cyan), showing the non-uniform distribution of lipid droplets across the PP-PC axis. **(B)** RNA levels of key lipogenesis enzymes in spatially sorted hepatocytes. The bar graph shows three independent experiments.

(C) Protein abundance of key lipogenesis enzymes identified in the proteomics. Data presented as mean ± SD. ns, **p <0.05, **p < 0.01, ***p < 0.001.

Figure 4. Mitochondrial morphology and organization across the lobule. (A) Confocal image of the PP-PC axis in liver sections from Mito-Dendra2 transgenic mice. Mitochondria are shown in white, and actin was labeled with phalloidin in red. Enlarged insets of a representative PP (left) and PC (right) cell are shown. **(B-C)** Mitochondria were visualized by 3D high-resolution confocal imaging and analyzed using Imaris. Mitochondrial surfaces were generated in PP (left) and PC (right) cells. Inset shows a representative mitochondrion with distinct morphological features. **(D)** Mitochondrial sphericity index (a measure of similarity to a perfect circle (=1)) of 3-5 cells was analyzed per group. **(E)** Mitochondrial counts per cell, using the mitochondrial surfaces generated in Imaris, were analyzed per group (3-5 cells). **(F)** Quantification of relative mtDNA copy number by qPCR in spatially sorted hepatocytes. The bar graph shows four independent experiments. **(G)** Quantification of mitochondrial volume frequency per cell using the mitochondrial surfaces generated in Imaris. **(H)** The abundance of VDAC1-3 proteins discovered in the proteomics is shown in box and whisker plots. **(I)** Mitochondrial mass was measured by flow cytometry of hepatocytes labeled with MitoTracker Green, E-cadherin, and CD73 to distinguish between PP and PC hepatocytes. A representative experiment is shown. Data presented as mean ± SD. ** p < 0.01, ****p < 0.0001.

Figure S3. Mitochondrial morphologies are conserved in the human liver. Confocal images of fixed human liver sections labeled with phalloidin (actin; yellow) and TOM20 (outer mitochondrial membrane; green). Insets of representative PP and PC hepatocytes show distinct morphological features (arrows).

Figure 5. PP mitochondria display higher turnover via mitophagy. (A) Intravital microscopy of transgenic mice expressing mtKeima, a pH-sensitive mitophagy reporter. The ratio between the 440 nm (green; neutral pH) and 560 nm (red; acidic pH) excitation measures the proportion of

mitochondria undergoing mitophagy. Insets (on the right) are magnified PP and PC regions of the lobule. **(B)** Quantification of mitophagy in PP and PC regions expressed as a fold change relative to PC cells. Mice were injected with saline or leupeptin to block lysosomal degradation. The bar graphs show four independent experiments. **(C)** The abundance of mitophagy-related proteins discovered in the proteomics is shown in the box and whisker plots. FUN14 Domain Containing 1 (FUNDC1); Bcl2 interacting protein 3 (Bnip3); BCL2 Like 13 (Bcl2l13); GABA type A receptor-associated protein-like 2 (Gabarapl2); GABA type A receptor-associated protein like (Gabarapl). Data presented as mean ± SD. ns, *$p < 0.05$, ****$p < 0.0001$.

Figure S4. PP mitochondria display higher turnover via mitophagy. (A) LC3-I and LC3-II levels were detected by western blot in liver lysates from fed or fasted mice treated with saline or leupeptin. **(B)** Confocal microscopy of liver sections from mice transduced with Cox8-EGFP-mCherry adenovirus. Representative PP and PC cells are shown from saline or leupeptin-treated mice. **(C)** The Cox8-EGFP-mCherry reporter was used to measure mitophagy by calculating the percent of the mitophagosome area normalized to the whole cell area in saline or leupeptin-treated mice. The bar graph shows 15-20 cells quantified from 3 mice. Data presented as mean ± SD. ns, ***$p < 0.001$.

Figure 6. Phosphoproteome highlights spatially regulated pathways contributing to mitochondrial phenotypes. (A) Overview of phosphopeptides, phosphosites, and phosphoproteins identified in the phosphoproteome. **(B)** The proportion of phosphorylated serine (p-S), threonine (p-T), and tyrosine (p-Y) residues in the identified phosphopeptides. **(C)** The proportion of proteins identified with a certain number of phosphorylated residues per protein. **(D)** The number of phosphosites with a PP, PC, or unzonated (UZ) bias is shown in the bar graph. **(E-F)** The PP or PC zonated phosphoproteins were analyzed using GO enrichment analysis. **(G)** Mitochondrial phosphoproteome is shown in a volcano plot with $\log_2$ PC/PP fold-change (*x-axis*) and the $-\log_{10}$ p-value (y-axis). **(H)** Selected zonated mitochondrial phosphoproteins are shown in the table, including the phosphosites identified and the protein's cellular function. Dash and comma marks distinguish between potential and identified sites.

Figure S5. Comparative phosphoproteome in spatially sorted hepatocytes. (A) Principal component analysis (PCA) and **(B)** frequency histogram of phosphorylated peptides. Correlation Matrix Heatmap of the phosphoproteome data set. **(C)** Volcano plot showing the $\log_2$ *PC/*PP fold-change (x-axis) and the $-\log_{10}$ p-value (y-axis).

Figure 7. Nutrient sensing signaling regulates mitochondrial functional and morphological diversity. (A-C) AMPK or mTOR signaling was modulated *in vivo* by injecting an activating drug, AICAR or MHY1485, or an inhibitory drug Cpc or Torin, respectively. The impact on mitochondrial phenotypes was evaluated using flow cytometry **(A)** mitochondrial membrane potential with JC-1 **(B)** mitochondrial volume with MitoTracker Green **(C)** and lipid droplets with BODIPY. Bar graphs show 3-5 independent experiments. **(D)** Confocal images of hepatocytes from liver sections of Mito-Dendra2 mice treated with vehicle, AICAR, or MHY1485. Mitochondria are shown in white, and phalloidin outlines hepatocytes in red. Scale bar= 3um. **(E)** Mitochondrial sphericity in mice treated with vehicle, AICAR, or MHY1485 was quantified. Data are presented as mean. ns, *$p < 0.05$, **$p < 0.01$, ***$p < 0.001$, ****$p < 0.0001$.

Figure S6. Nutrient sensing signaling regulates mitochondrial heterogeneity. (A) Determination of AICAR and Compound C (CpC) concentrations for *in vivo* modulation of AMPK signaling. Drug efficacy was evaluated by Western blotting for pACC1 (S79) levels. **(B)** Determination of MHY1485 and Torin concentrations for *in vivo* modulation of mTOR signaling. Drug efficacy was evaluated by Western blotting for p4EBP1(Thr37/Thr46) levels. **(C)** Mice were treated with two doses of vehicle, AMPK inhibitor (Compound C) or activator (AICAR), or mTOR inhibitor (Torin I) or activator (MHY1485). Graphs show the evaluation of drug effect on cell size measured by flow cytometry n = 3-5 independent experiments. Data presented as mean ± SD. ns, *$p < 0.05$, **$p < 0.01$, ***$p < 0.001$, ****$p < 0.0001$.

Movie S1. High resolution z-stack of PP mitochondria

Movie S2. High resolution z-stack of PC mitochondria

Movie S3. 3D volume rendering of PP mitochondria

Movie S4. 3D volume rendering of PC mitochondria

Animal experiments

Experiments were approved by the Institutional Animal Care and Use Committee of the National Cancer Institute and in compliance with the Guide for the Care and Use of Laboratory Animals (National Institutes of Health publication 86-23, revised 1985). All experiments were conducted on ad libitum-fed, eight-to-ten weeks old C57BL/6J (strain# 000664), mtKeima [28] or PhAMexcised (photo-activatable mitochondria; strain# 018397) male mice obtained from Jackson Laboratories.

Intra-cardiac fixation, tissue processing, and immunofluorescence

Mice were anesthetized with 250 mg/kg Xylazine and 50 mg/kg Ketamine (diluted in saline) injected intraperitoneally (i.p.). The liver was fixed by transcardial perfusion of ice-cold PBS for 2 min followed by ice-cold 4% paraformaldehyde (PFA) in PBS at a rate of 5 ml/min. Livers were harvested and stored in 4% PFA in PBS overnight and processed in a sucrose gradient before embedding in OCT (Tissue-Tek). Blocks were kept at -80 °C until 10 μm thick slices were made with a cryostat and slides prepared. Slides were stored at -80 °C until thawed, rehydrated, and blocked with 0.1% Triton X-100 and 10% FBS in PBS for 1 h at room temperature. Next, slides were incubated with primary antibody at 4 °C overnight. The following day, the slides were washed three times, 15 min each, and then incubated with a secondary antibody for 1 h at room temperature. After three 15 min washes, slides were mounted with Fluoromount-G and a coverslip (#1).

Confocal microscopy and imaging analysis for mitochondrial morphology

Tile scans and z stacks were acquired using a Leica SP8 inverted confocal laser scanning microscope using a 63x oil objective and a 1.4 numerical aperture. Images were deconvolved using the LIGHTNING module in LAS X. Mitochondria surfaces and measurements (count, sphericity, and volume) were generated using Imaris (Bitplane 9.9.0).

Human tissue was obtained under an NIH IRB-approved protocol (13-C-0076) for risk-reducing surgery performed on patients with germline genetic mutation(s). All tissue procured, which included liver samples used in this study, were grossly normal as determined by the surgeon and histopathologically normal as determined by a board-certified pathologist. Of note, all tissue was obtained within 20 min of the skin incision.

Measurement of mitochondrial membrane potential via intravital microscopy

Intravital microscopy was performed as previously described [45]. Mitotracker Green FM(250 μM) and tetramethylrhodamine ethyl ester (TMRE) (200 μM) were consecutively injected retro-orbitally to label mitochondria with/without mitochondrial membrane potential. After 30 min of incubation for each dye, the liver was exposed on the microscope stage under anesthesia, and images acquired using excitation at 440 nm and 560 nm. The fluorescence intensity of TMRE and Mitotracker Green FM was analyzed across the PP-PC axis through line scanning.

Measurements of mitophagy

Mitophagy was measured in mtKeima mice [28] or C57BL/6J mice injected with Ad-Cox8-EGFP-mCherry ($1x10^9$ PFU diluted in 200 μl of PBS) [29] using intravital microscopy as previously described [45]. lysosome inhibitor leupeptin (80 mg/kg), or saline was injected i.p. 16 h prior to the experiment. A second dose of leupeptin (40 mg/kg) or saline was administered 12 h later. Three to five mice were analyzed per experiment.

Western blot analysis

Proteins from primary hepatocytes or whole liver were extracted by homogenization in RIPA lysis buffer (150 mM NaCl, 0.1% Triton X-100, 0.5% sodium deoxycholate, 0.1% sodium dodecyl sulfate, and 50 mM Tris HCl pH 8.0) containing EDTA, PMSF, and Halt Inhibitor Cocktail (Thermo Fisher), followed by centrifugation at 13,000 rpm at 4 °C for 30 min. Protein concentration was

determined using a Pierce™ BCA Protein Assay Kit (Thermo Fisher). Lysates were boiled at 95 °C for 5 min, and 5-10 μg aliquots were fractionated by SDS-PAGE and then transferred to nitrocellulose 0.45 μm membrane (Bio-Rad). Membranes were blocked for 1 h at room temperature in 5% BSA in 1x Tris-buffered saline + 0.1% Tween 20 (TBST), then incubated with primary antibody diluted in 5% BSA in 1x TBST at 4 °C overnight. Membranes were washed three times with TBST and then incubated in the secondary antibody 1 h at room temperature. Membranes were washed three times with TBST, followed by Clarity ECL western blot substrate solution (Bio-Rad) was applied for detection and imaged using the ChemiDoc Imaging System (Bio-Rad). Bands were quantified with ImageJ.

Liver Perfusion and hepatocyte isolation

Livers of anesthetized mice were perfused by inserting a 22-gauge syringe into the portal vein and delivering 25 ml of pre-warmed (37 °C) perfusion buffer [Krebs-Henseleit buffer (Sigma) with 0.5 μM EDTA], followed by 25 ml collagenase A buffer [Krebs-Henseleit buffer, with 0.1 mM Ca_2Cl and 0.4 mg/ml collagenase A (Sigma)]. After perfusion, livers were transferred into a Petri dish, flooded with cold PBS, and hepatocytes gently released using forceps. Dissociated cells were collected and filtered through a 100 μm cell strainer. Cells were centrifuged at 50 rpm for 5 min at 4 °C to obtain a hepatocyte-enriched pellet. Pellets were resuspended in cold PBS, filtered through a 40 μm cell strainer, and centrifuged at 50 rpm for 5 min at 4 °C. Percoll diluted in 10x Hank's buffer (Sigma) was added to the cell suspension and centrifuged at 50 rpm for 5 min at 4 °C. The supernatant containing dead cells was removed by aspiration. The pellet was resuspended in cold PBS, and the cell number was determined.

Fluorescence-activated cell sorting (FACS) of PP and PC populations.

Cell sorting was performed on a FACSAria Fusion cell sorter (BD Biosciences). Forward and side light scatter was used to distinguish cells from debris and to identify single cells. Zombie-Green fixable live dead dye (1:500, BioLegend) was used to discriminate between live and dead cells. The PP and PC populations were identified using anti-E-cadherin-PE and anti-CD73-APC antibody

staining (1:150; BioLegend). The PP- and PC-specific gates were set after spectral compensation using appropriate fluorescent minus (FMO) controls.

Protein Digestion and TMT labeling

Cells were lysed in 50 mM HEPES, pH 8.0, 8M urea, and 10% methanol, followed by sonication. Lysates were clarified by centrifugation, and protein concentration was quantified using a BCA protein estimation kit (Thermo Fisher). A 250 ug was alkylated and digested by incubating overnight at 37°C in trypsin at a ratio of 1:50 (Promega). Digestion was acidified by adding formic acid (FA) to a final concentration of 1% and desalted using Pierce peptide desalting columns according to the manufacturer's protocol. Peptides were eluted from the column using 50% ACN/0.1% FA, dried in a speed vac and kept frozen at -20°C for further analysis.

For TMT labeling, 125 ug of each sample was reconstituted in 50 μl of 50 mM HEPES, pH 8.0, 500 ug of TMTpro-16plex label (Thermo Fisher) in 100% ACN. After incubating the mixture for 1 h at room temperature with occasional mixing, the reaction was terminated by adding 8 μl of 5% hydroxylamine. As there were more than 16 samples, we generated a pooled sample consisting of equal amounts of lysate from each condition and TMT labeled. The pool was added to each TMT experiment. The TMT-labeled peptides were pooled and dried in a speed vac. The samples were desalted, and excess TMT labels were removed using peptide desalting columns (Thermo Fisher). A 100 ug aliquot of labeled peptide mixture was fractionated using high pH reversed-phase, and the remaining peptide mixture was used for phospho-enrichment.

Phosphopeptide enrichment

Phosphopeptides were enriched from the TMT-labeled peptides using the SMOAC (Sequential enrichment of Metal Oxide Affinity Chromatography) method. First, the phosphopeptides were enriched using the HiSelect TiO_2 phosphopeptide enrichment kit (Thermo Fisher) according to the manufacturer's protocol. The flow-through and wash from the TiO_2 enrichment kit were then combined and enriched using the HiSelect Fe-NTA phosphopeptide enrichment kit (Thermo Fisher). The enriched phosphopeptides obtained by both methods were dried by speed vac and stored at -20 °C until analysis by mass spectrometry.

High pH reversed-phase fractionation.

The first-dimensional separation of peptides was performed using a Waters Acquity UPLC system coupled with a fluorescence detector (Waters) using a 150 mm x 3.0 mm Xbridge Peptide BEM™ 2.5 μm C18 column (Waters) operating at 0.35 ml/min. The dried peptides were reconstituted in 100 μl of mobile phase A solvent (3 mM ammonium bicarbonate, pH 8.0). Mobile phase B was 100% acetonitrile (Thermo Fisher). The column was washed with mobile phase A for 10 min followed by gradient elution 0- 50% B (10-60 min) and 50-75 %B (60-70 min). Fractions were collected every minute. These 60 fractions were pooled into 24 fractions. Fractions were vacuum centrifuged, and lyophilized fractions were stored at -80°C until analysis by mass spectrometry.

Mass Spectrometry acquisition

The lyophilized peptide fractions were reconstituted in 0.1% TFA and subjected to nanoflow liquid chromatography (Thermo Ultimate™ 3000RSLC nano LC system, Thermo Fisher) coupled to an Orbitrap Eclipse mass spectrometer (Thermo Fisher). Peptides were separated using a low pH gradient and 5-50% ACN over 120 min in a mobile phase containing 0.1% formic acid at a 300 nl/min flow rate. MS scans were performed in the Orbitrap analyzer at a resolution of 120,000 with an ion accumulation target set at $4e^5$ and max IT set at 50ms over a mass range of 400-1600 m/z. Ions with a determined charge state between 2 and 5 were selected for MS2 scans in the ion trap with CID fragmentation (Turbo; NCE 35%; maximum injection time 35 ms; AGC 1×10^4). The spectra were searched using the Real Time Search Node in the tune file using mouse Uniprot database using Comet search algorithm with TMT16 plex (304.2071Da) set as a static modification of lysine and the N-termini of the peptide. Carbamidomethylation of cysteine residues (+57.0214 Da) was set as a static modification, while oxidation of methionine residues (+15.9949 Da) was set up as a dynamic modification. For the selected peptide, an SPS–MS3 scan was performed using up to 10 *b*- and *y*-type fragment ions as precursors in an Orbitrap at 50,000 resolution with a normalized AGC set at 500 followed by maximum injection time set as “Auto” with a normalized collision energy setting of 65.

The enriched phospho-samples were reconstituted in 0.1% TFA and analyzed using an Orbitrap Eclipse mass spectrometer. Peptides were separated using a low pH gradient, and FAIMS was enabled during data acquisition with the compensation voltages set at -45V, -60V, and -75V set up at the first run, -50V, -65V, and -80V for the second run and -55V, -70V and -85 V for the last run. MS scans were performed in the Orbitrap analyzer at a resolution of 120,000 with an ion accumulation target set at $4e^5$ and max IT set at 50ms over a mass range of 350-1600 m/z. Ions with a known charge state between 2 and 6 were selected for MS2 scans. A cycle time of 1 sec was used for each CV, and a quadrupole isolation window of 0.4 m/z was used for MS/MS analysis. An Orbitrap at 15,000 resolution with a normalized AGC set at 250 followed by maximum injection time set as "Auto" with a normalized collision energy setting of 38 was used for MS/MS analysis. The node "Turbo TMT" was switched on for the high-resolution acquisition of TMT reporter ions.

Data Analysis

Acquired MS/MS spectra were searched against the mouse Uniprot protein database and a contaminant protein database using SEQUEST in the Proteome Discoverer 2.4 software (Thermo Fisher). The precursor ion tolerance was set at 10 ppm, and the fragment ions tolerance was set at 0.02 Da, with methionine oxidation included as a dynamic modification. For the phospho-enriched samples, serine, threonine, and tyrosine phosphorylation were set as variable modifications. Carbamidomethylation of cysteine residues and TMTpro16 plex (304.2071 Da) was set as static modification of lysine and the N-terminus of the peptide. Trypsin was specified as the proteolytic enzyme, with up to 2 missed cleavage sites allowed. Searches used a reverse sequence decoy strategy to control for the false peptide discovery, and identifications were validated using the Percolator algorithm in Proteome Discoverer 2.4.

Reporter ion intensities were adjusted to correct for lot-specific impurities according to the manufacturer specification, and the abundances of the proteins were quantified using the summation of the reporter ions for all identified peptides. A two-step normalization procedure was applied to a 24-plex TMT experiment [2 TMT experiments with 12 samples each]. First, the reporter abundances were normalized across all the channels to account for equal peptide

loading. Secondly, the intensity from the pooled sample was used to normalize the batch effect from the multiple TMT experiments. Samples were further normalized using the Voom algorithms and quantile normalization from the Limma R package (v3.40.6). Differential peptide expression analysis was performed using Limma, where zonation was determined by the p-value (0.05) and FC (≥1.2). Pathway enrichment analysis was performed using Fisher's Exact test with GO database. GraphPad Prism 9 and Biorender were used for visualization.

Seahorse assay

A Seahorse XFe96 Analyzer and XF Mito Stress Test Kit (Agilent Technologies) were used to measure the oxygen consumption rate (OCR) and extracellular acidification rate (ECAR) of PP and PC-sorted cells. A day before the assay, the cartridge sensor was hydrated overnight with Seahorse Bioscience Calibration Solution at 37 °C without CO_2. After sorting, cells were seeded in a 96-well seahorse plate at a 5.0 × 104 cells/well density and allowed to adhere for 2 h. After 2 h, cell media was replaced with serum-free Seahorse XF Base media containing glucose, pyruvate, and glutamine (pH 7.4), and the cells were incubated at 37 ˚C in a non-CO_2 incubator for 1 h. OCR and ECAR were measured after the injection of oligomycin (1.5 μM), FCCP (1 μM), and rotenone/antimycin (0.5 μM). In addition to XF Mito Stress Test Kit, the XF Mito Fuel kit was used together includes three inhibitors, UK5099 (2 μM), BPTES (3 μM), and etomoxir (4 μM), to measure the dependency of cells on the three primary mitochondrial fuels; glucose, glutamine, and long-chain fatty acids, respectively. Four independent experiments were conducted with six to eight replicates per population and treatment condition per experiment. All data were normalized to BCA (Thermo Fisher). Measurements for basal respiration and maximum respiration capacity were presented as a percentage normalized to PP.

ATP measurement

The bioluminescence ATP assay kit was used according to manufacturer instructions (Invitrogen) to analyze spatially sorted hepatocytes. ATP levels were calculated according to cell number of then normalized to PP cells.

Citrate Synthase activity assay

Citrate Synthase (CS) activity was analyzed following the manufacturer protocol (Abcam). After collecting the cells via FACS, cells were lysed. Next, a 50 µl aliquot of supernatant or standard GSH solution with 50 µl of reaction buffer was added per well in a 96-well plate to measure the absorbance (OD 412 nm) in kinetic mode at 25 °C for 40 min. CS activity was calculated based on two different time points considering the dilution factor and cell number, then normalized to the PP fraction.

DNA and RNA isolation

RNA was isolated from spatially sorted cells using the RNeasy mini kit and QIAshredder homogenizer columns (Qiagen). Total DNA was isolated using the DNeasy Blood and Tissue kit (Qiagen).

Quantitative PCR

A High-Capacity RNA to cDNA kit (Thermo Fisher) was used to synthesize random-primed cDNA from 600 ng DNAse treated RNA. Real-time PCR was conducted in 384 well-plates using a ViiA7 Real-time PCR system (Applied Biosystems). Singleplex reactions (10 µl) containing a FAM-MGB expression assay for the gene of interest (Acaca Mm01304289_m1, Acly Mm01302282_m1, Fasn Mm00662319_m1, Scd1 Mm00772290_m1) or endogenous control (Ppia Mm02342430_g1) (Thermo Fisher) were performed using cDNA synthesized from 3ng RNA and 1x Fast Advanced Master Mix (Thermo-without Amp Erase UNG). The comparative Ct method (delta, delta Ct) was used to determine relative expression normalized to Ppia (Applied Biosystems® ViiA™ 7Real-Time PCR System Getting Started Guides).

mtDNA copy number determination

Mitochondrial DNA content was measured by comparing the DNA copy number of two mitochondrial encoded genes (ND1 and 16S rRNA) to HK, a nuclear-encoded gene (Curr Protoc Mouse Biol, 7(1): 47–54). The mitochondrial to nuclear DNA ratio (mtDNA/nDNA) was determined by Real-time PCR using an ABI Viia7 Real-Time PCR System (Applied Biosystems).

Because mitochondrial genes lack introns, it was possible to use TaqMan gene expression assays for mtDNA copy number. Singleplex reactions (10 μl) containing FAM-MGB assays for ND1 Mm04225274_s1, Rnr2 Mm04260181_s1, or HK2 Mm00193901_cn (Applied Biosystems) were performed in quadruplicate using 384 well plates with 10 ng DNA and 1x Universal Master Mix (Applied Biosystems-without Amp Erase UNG). Determination of mtDNA content was performed using the comparative Ct method (delta, delta Ct) with normalization to HK2 as an internal reference (Applied Biosystems® ViiA™ 7Real-Time PCR System Getting Started Guides).

Drug treatment and flow cytometry assay

Mice were treated with two doses of either vehicle, Compound C (CpC, 20 mg/kg), 5-Aminoimidazole-4-carboxamide ribonucleotide (AICAR, 0.5 mg/kg), Torin I (20 mg/kg) or MHY1485 (20 mg/kg) before primary hepatocytes were isolated via perfusion. Hepatocytes were then labeled with Cy-PE/PE-anti-E-cadherin and APC-anti-CD73 and either JC1 (5 μM), BODIPY-493/503 (2 μM), or Mitotracker Green FM (200 nM) (Thermo Fisher) and incubated at 37 °C for 15-30 min. The fluorescent signal was measured by BD LSRFortessa (BD Biosciences) cell analyzer. Consistent with FACS, forward and side light scatter was used to distinguish cells from debris and to identify single cells.

1 Picard, M. & Shirihai, O. S. Mitochondrial signal transduction. *Cell Metab* **34**, 1620-1653 (2022). https://doi.org:10.1016/j.cmet.2022.10.008

2 Glancy, B. Visualizing Mitochondrial Form and Function within the Cell. *Trends Mol Med* **26**, 58-70 (2020). https://doi.org:10.1016/j.molmed.2019.09.009

3 Hoppins, S. The regulation of mitochondrial dynamics. *Curr Opin Cell Biol* **29**, 46-52 (2014). https://doi.org:10.1016/j.ceb.2014.03.005

4 Friedman, J. R. & Nunnari, J. Mitochondrial form and function. *Nature* **505**, 335-343 (2014). https://doi.org:10.1038/nature12985

5 Westermann, B. Bioenergetic role of mitochondrial fusion and fission. *Biochim Biophys Acta* **1817**, 1833-1838 (2012). https://doi.org:10.1016/j.bbabio.2012.02.033

6 Niemi, N. M. & Pagliarini, D. J. The extensive and functionally uncharacterized mitochondrial phosphoproteome. *Journal of Biological Chemistry* **297** (2021). https://doi.org:ARTN 100880
10.1016/j.jbc.2021.100880

7 Kolitsida, P. *et al.* Phosphorylation of mitochondrial matrix proteins regulates their selective mitophagic degradation (vol 116, pg 20517, 2019). *P Natl Acad Sci USA* **116**, 24374-24374 (2019). https://doi.org:10.1073/pnas.1918594116

8 Grimsrud, P. A. *et al.* A quantitative map of the liver mitochondrial phosphoproteome reveals posttranslational control of ketogenesis. *Cell Metab* **16**, 672-683 (2012). https://doi.org:10.1016/j.cmet.2012.10.004

9 Jungermann, K. in *Regulation of Hepatic Metabolism: Intra- and Intercellular Compartmentation* (eds Ronald G. Thurman, Frederick C. Kauffman, & Kurt Jungermann) 445-469 (Springer US, 1986).

10 Cunningham RP, P.-S. N. Liver Zonation – Revisiting Old Questions With New Technologies. *Front. Physiol.* (2021). https://doi.org:10.3389

11 Brosch, M. *et al.* Epigenomic map of human liver reveals principles of zonated morphogenic and metabolic control. *Nat Commun* **9**, 4150 (2018). https://doi.org:10.1038/s41467-018-06611-5

12 Halpern, K. B. *et al.* Single-cell spatial reconstruction reveals global division of labour in the mammalian liver. *Nature* **542**, 352-356 (2017). https://doi.org:10.1038/nature21065

13 Novikoff, A. B. Cell heterogeneity within the hepatic lobule of the rat: staining reactions. *J Histochem Cytochem* **7**, 240-244 (1959). https://doi.org:10.1177/7.4.240

14 Deane, H. W. A cytological study of the diurnal cycle of the liver of the mouse in relation to storage and secretion. *Anat Rec* **88**, 39-65 (1944). https://doi.org:DOI 10.1002/ar.1090880104

15 JM, K. Comparative and experimental studies on the cytology of the liver. (1933).

16 Smith, D. M. THE ONTOGENETIC HISTORY OF THE MITO- CHONDRIA OF THE HEPATIC CELL OF THE WHITE RAT. (1931).

17 Ben-Moshe, S. *et al.* Spatial sorting enables comprehensive characterization of liver zonation. *Nat Metab* **1**, 899-911 (2019). https://doi.org:10.1038/s42255-019-0109-9

18 Weigert, R., Porat-Shliom, N. & Amornphimoltham, P. Imaging cell biology in live animals: ready for prime time. *J Cell Biol* **201**, 969-979 (2013). https://doi.org:10.1083/jcb.201212130

19 Fang, M. & Lowenstein, J. M. Citrate and the conversion of carbohydrate into fat. The regulation of fatty acid synthesis by rat liver extracts. *Biochem J* **105**, 803-811 (1967). https://doi.org:10.1042/bj1050803

20 Shepherd, D. & Garland, P. B. The kinetic properties of citrate synthase from rat liver mitochondria. *Biochem J* **114**, 597-610 (1969). https://doi.org:10.1042/bj1140597

21 Massalha, H. *et al.* A single cell atlas of the human liver tumor microenvironment. *Mol Syst Biol* **16** (2020). https://doi.org:ARTN e9682
10.15252/msb.20209682

22 Pham, A. H., McCaffery, J. M. & Chan, D. C. Mouse lines with photo-activatable mitochondria to study mitochondrial dynamics. *Genesis* **50**, 833-843 (2012). https://doi.org:10.1002/dvg.22050

23 Macleod, K. F. Mitophagy and Mitochondrial Dysfunction in Cancer. *Annu Rev Canc Biol* **4**, 41-60 (2020). https://doi.org:10.1146/annurev-cancerbio-030419-033405

24 Palikaras, K., Lionaki, E. & Tavernarakis, N. Mechanisms of mitophagy in cellular homeostasis, physiology and pathology. *Nat Cell Biol* **20**, 1013-1022 (2018). https://doi.org:10.1038/s41556-018-0176-2

25 Han, S., Zhang, M., Jeong, Y. Y., Margolis, D. J. & Cai, Q. The role of mitophagy in the regulation of mitochondrial energetic status in neurons. *Autophagy* **17**, 4182-4201 (2021). https://doi.org:10.1080/15548627.2021.1907167
26 Manella, G. & Asher, G. The Circadian Nature of Mitochondrial Biology. *Front Endocrinol (Lausanne)* **7**, 162 (2016). https://doi.org:10.3389/fendo.2016.00162
27 Jacobi, D. *et al.* Hepatic Bmal1 Regulates Rhythmic Mitochondrial Dynamics and Promotes Metabolic Fitness. *Cell Metab* **22**, 709-720 (2015). https://doi.org:10.1016/j.cmet.2015.08.006
28 Sun, N. *et al.* Measuring In Vivo Mitophagy. *Mol Cell* **60**, 685-696 (2015). https://doi.org:10.1016/j.molcel.2015.10.009
29 Ma, X. & Ding, W. X. A fluorescence imaging based-assay to monitor mitophagy in cultured hepatocytes and mouse liver. *Liver Res* **5**, 16-20 (2021). https://doi.org:10.1016/j.livres.2020.12.002
30 Droin, C. *et al.* Space-time logic of liver gene expression at sub-lobular scale. *Nat Metab* (2021). https://doi.org:10.1038/s42255-020-00323-1
31 Springer, M. Z. *et al.* BNIP3-dependent mitophagy promotes cytosolic localization of LC3B and metabolic homeostasis in the liver. *Autophagy* **17**, 3530-3546 (2021). https://doi.org:10.1080/15548627.2021.1877469
32 Niemi, N. M. *et al.* Pptc7 is an essential phosphatase for promoting mammalian mitochondrial metabolism and biogenesis. *Nature Communications* **10** (2019). https://doi.org:ARTN 3197
10.1038/s41467-019-11047-6
33 Ardito, F., Giuliani, M., Perrone, D., Troiano, G. & Lo Muzio, L. The crucial role of protein phosphorylation in cell signaling and its use as targeted therapy. *International Journal of Molecular Medicine* **40**, 271-280 (2017). https://doi.org:10.3892/ijmm.2017.3036
34 Gonzalez, A., Hall, M. N., Lin, S. C. & Hardie, D. G. AMPK and TOR: The Yin and Yang of Cellular Nutrient Sensing and Growth Control. *Cell Metab* **31**, 472-492 (2020). https://doi.org:10.1016/j.cmet.2020.01.015
35 Herzig, S. & Shaw, R. J. AMPK: guardian of metabolism and mitochondrial homeostasis. *Nat Rev Mol Cell Biol* **19**, 121-135 (2018). https://doi.org:10.1038/nrm.2017.95
36 Rambold, A. S., Kostelecky, B., Elia, N. & Lippincott-Schwartz, J. Tubular network formation protects mitochondria from autophagosomal degradation during nutrient starvation. *Proceedings of the National Academy of Sciences* **108**, 10190-10195 (2011). https://doi.org:doi:10.1073/pnas.1107402108
37 Ngo, J. *et al.* Mitochondrial morphology controls fatty acid utilization by changing CPT1 sensitivity to malonyl-CoA. *Embo J*, e111901 (2023). https://doi.org:10.15252/embj.2022111901
38 Benador, I. Y. *et al.* Mitochondria Bound to Lipid Droplets Have Unique Bioenergetics, Composition, and Dynamics that Support Lipid Droplet Expansion. *Cell Metabolism* **27**, 869-+ (2018). https://doi.org:10.1016/j.cmet.2018.03.003
39 Porat-Shliom, N., Harding, O. J., Malec, L., Narayan, K. & Weigert, R. Mitochondrial Populations Exhibit Differential Dynamic Responses to Increased Energy Demand during Exocytosis In Vivo. *iScience* **11**, 440-449 (2019). https://doi.org:10.1016/j.isci.2018.12.036

40 Tilokani, L. *et al.* AMPK-dependent phosphorylation of MTFR1L regulates mitochondrial morphology. *Sci Adv* **8**, eabo7956 (2022). https://doi.org:10.1126/sciadv.abo7956

41 He, Y. L. *et al.* BNIP3 phosphorylation by JNK1/2 promotes mitophagy via enhancing its stability under hypoxia. *Cell Death Dis* **13**, 966 (2022). https://doi.org:10.1038/s41419-022-05418-z

42 Poole, L. P., Bock-Hughes, A., Berardi, D. E. & Macleod, K. F. ULK1 promotes mitophagy via phosphorylation and stabilization of BNIP3. *Sci Rep* **11**, 20526 (2021). https://doi.org:10.1038/s41598-021-00170-4

43 Cho, Y. K. *et al.* STK3/STK4 signalling in adipocytes regulates mitophagy and energy expenditure. *Nat Metab* **3**, 428-441 (2021). https://doi.org:10.1038/s42255-021-00362-2

44 Rosenberger, F. A. *et al.* Spatial single-cell mass spectrometry defines zonation of the hepatocyte proteome. *bioRxiv*, 2022.2012.2003.518957 (2022). https://doi.org:10.1101/2022.12.03.518957

45 Stefkovich, M. L., Kang, S. W. S. & Porat-Shliom, N. Intravital Microscopy for the Study of Hepatic Glucose Uptake. *Curr Protoc* **1**, e139 (2021). https://doi.org:10.1002/cpz1.139

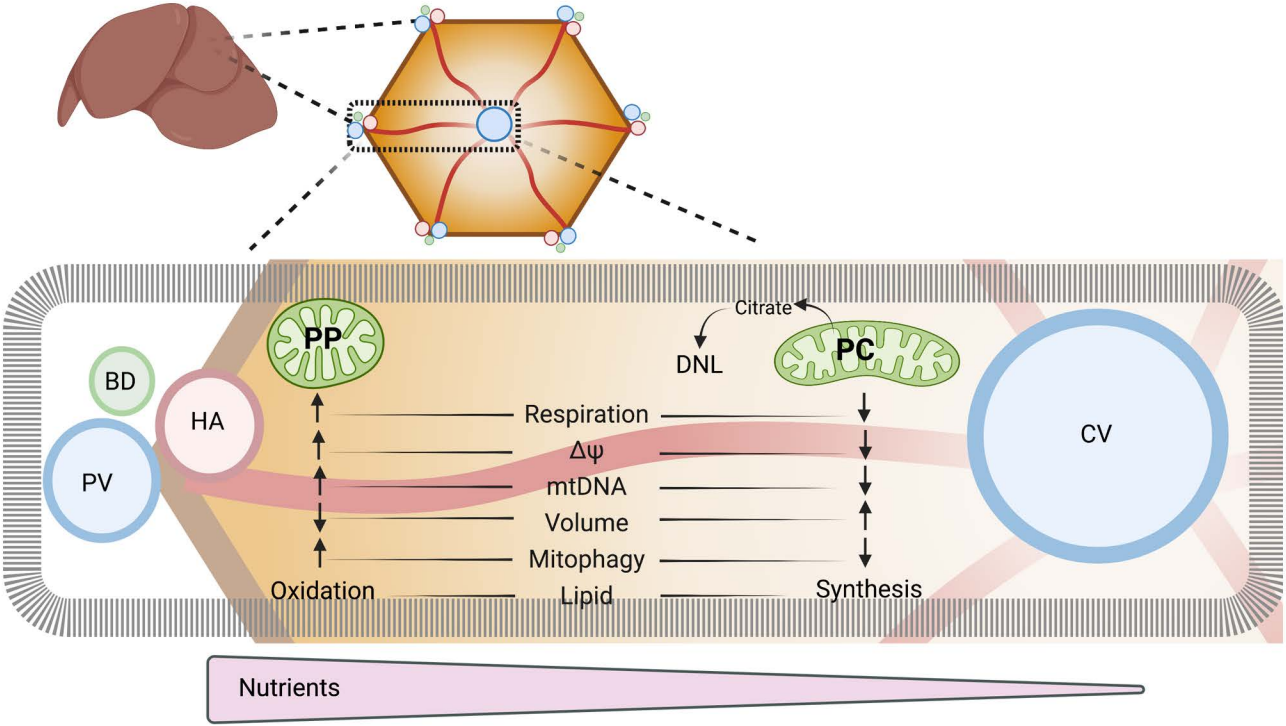

Graphical abstract Kang et al.

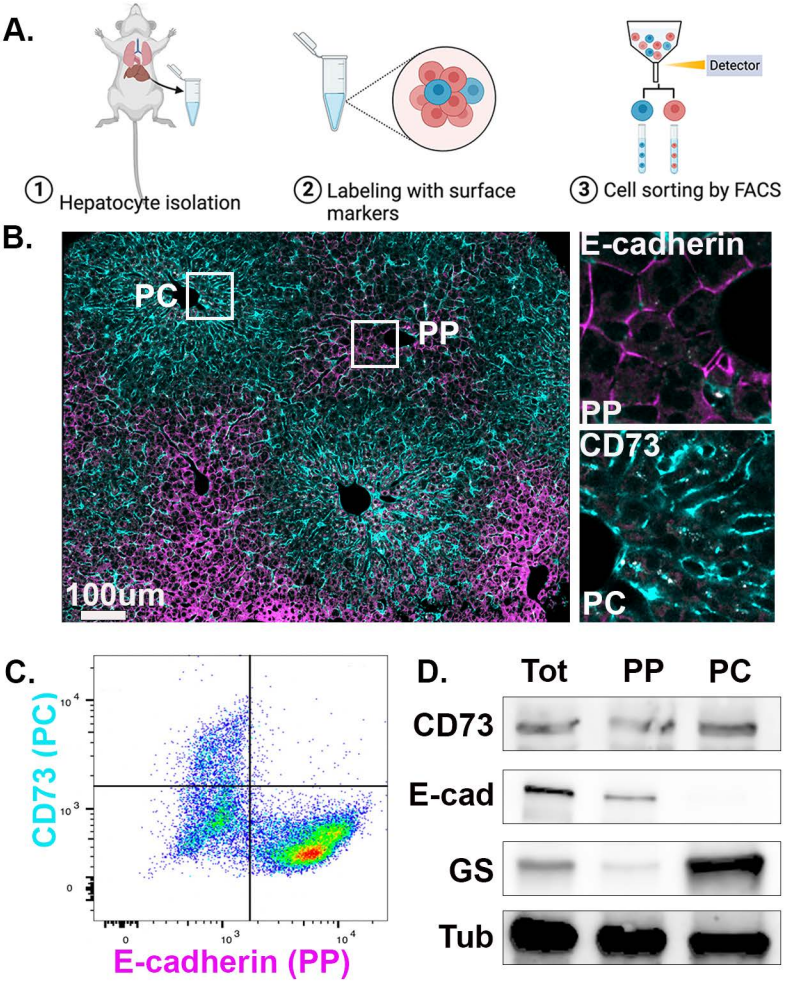

Fig 1. Spatial enrichment of PP and PC hepatocytes

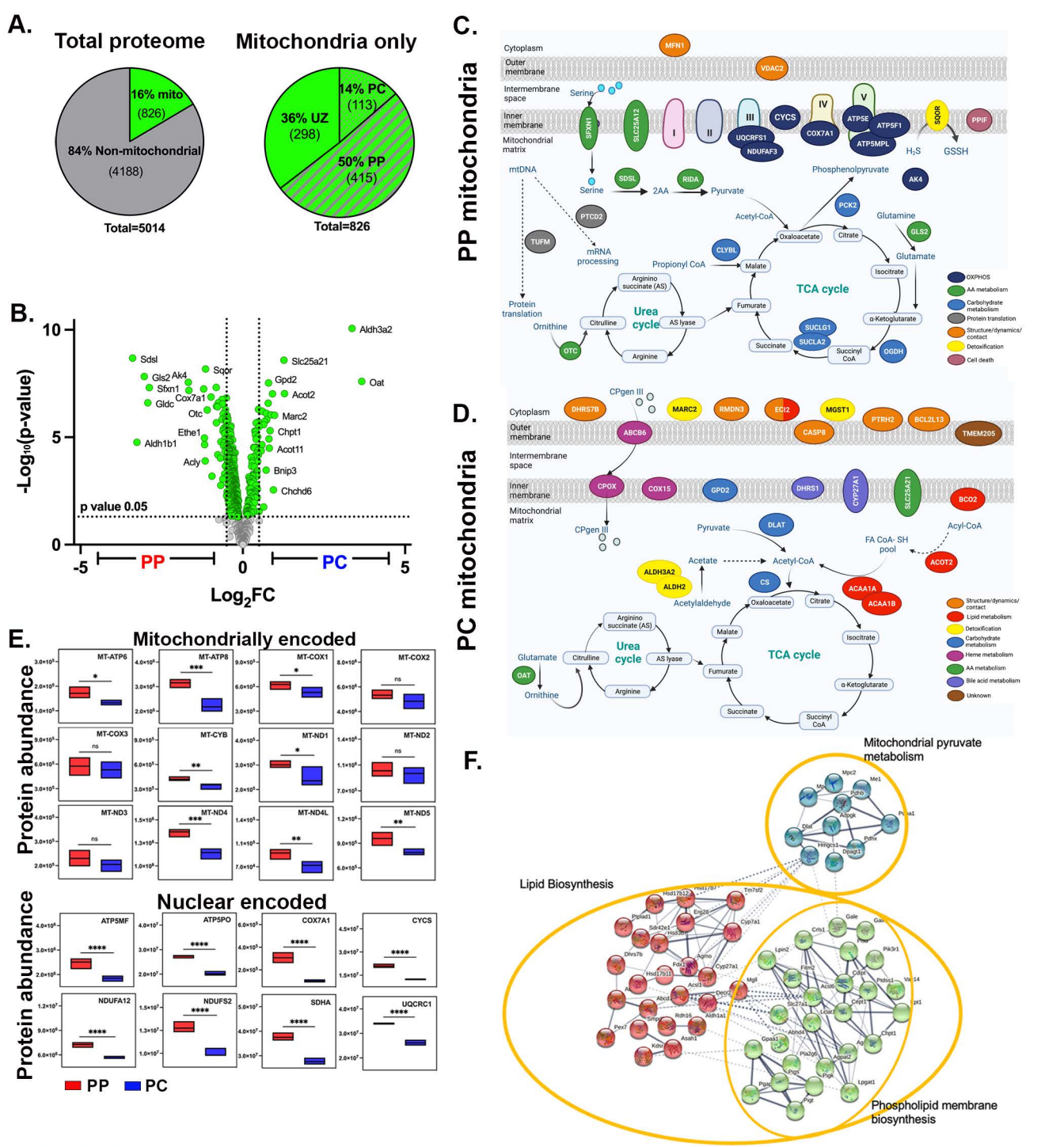

Fig 2. Spatial characterization of mitochondrial proteome

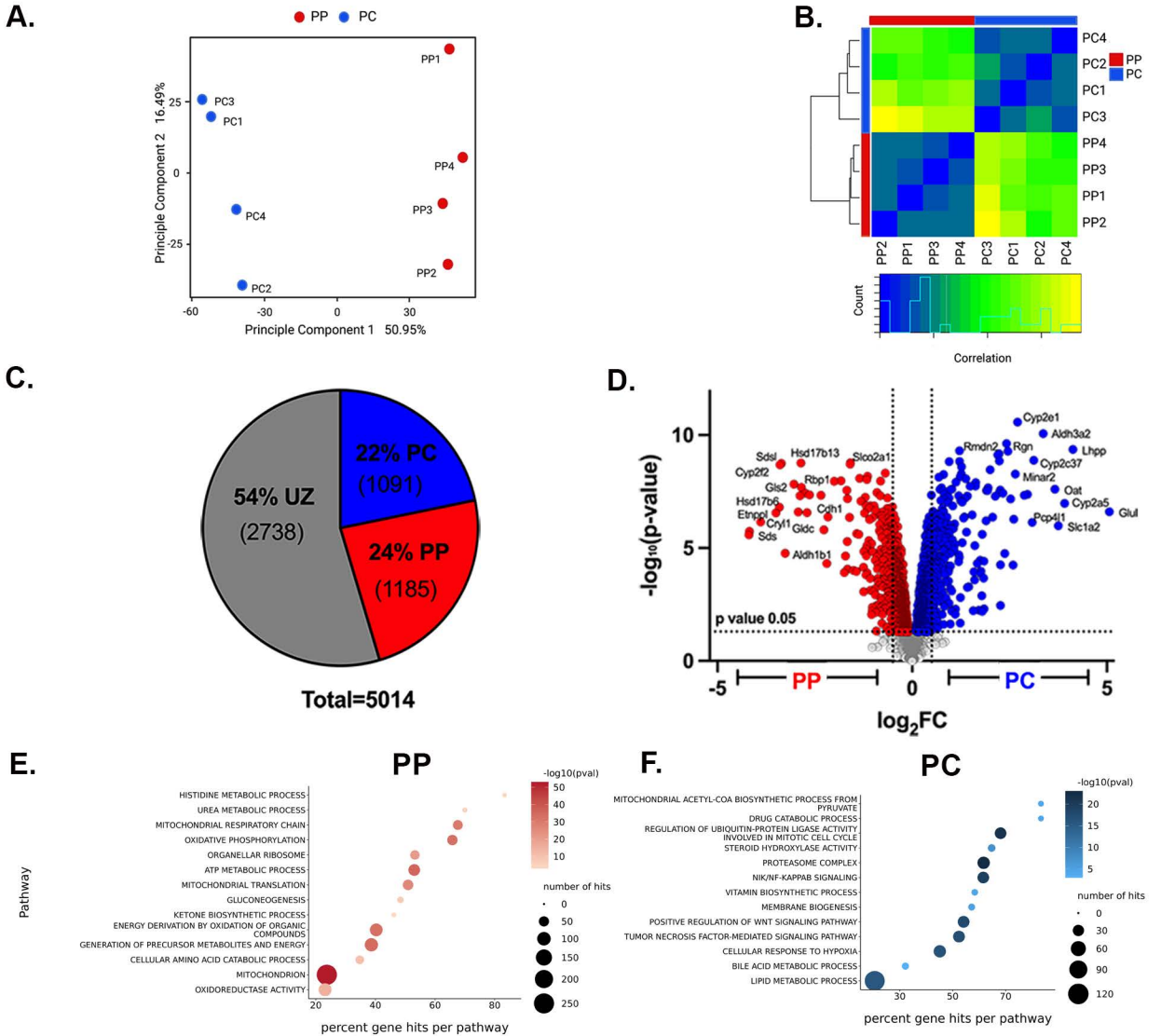

Fig S1 Hepatocyte spatial proteome

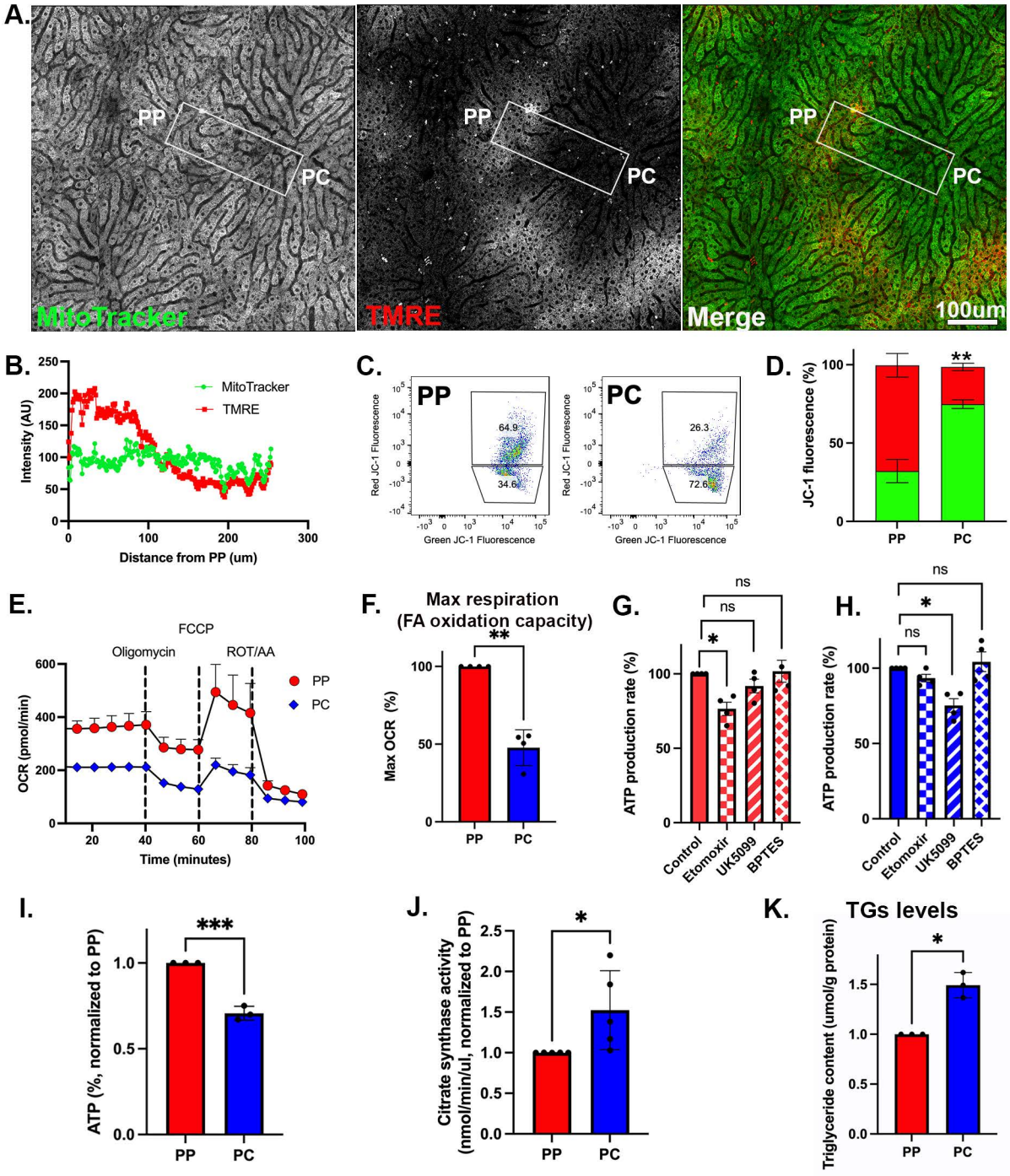

Fig 3. PP mitochondria display higher bioenergetic capacity

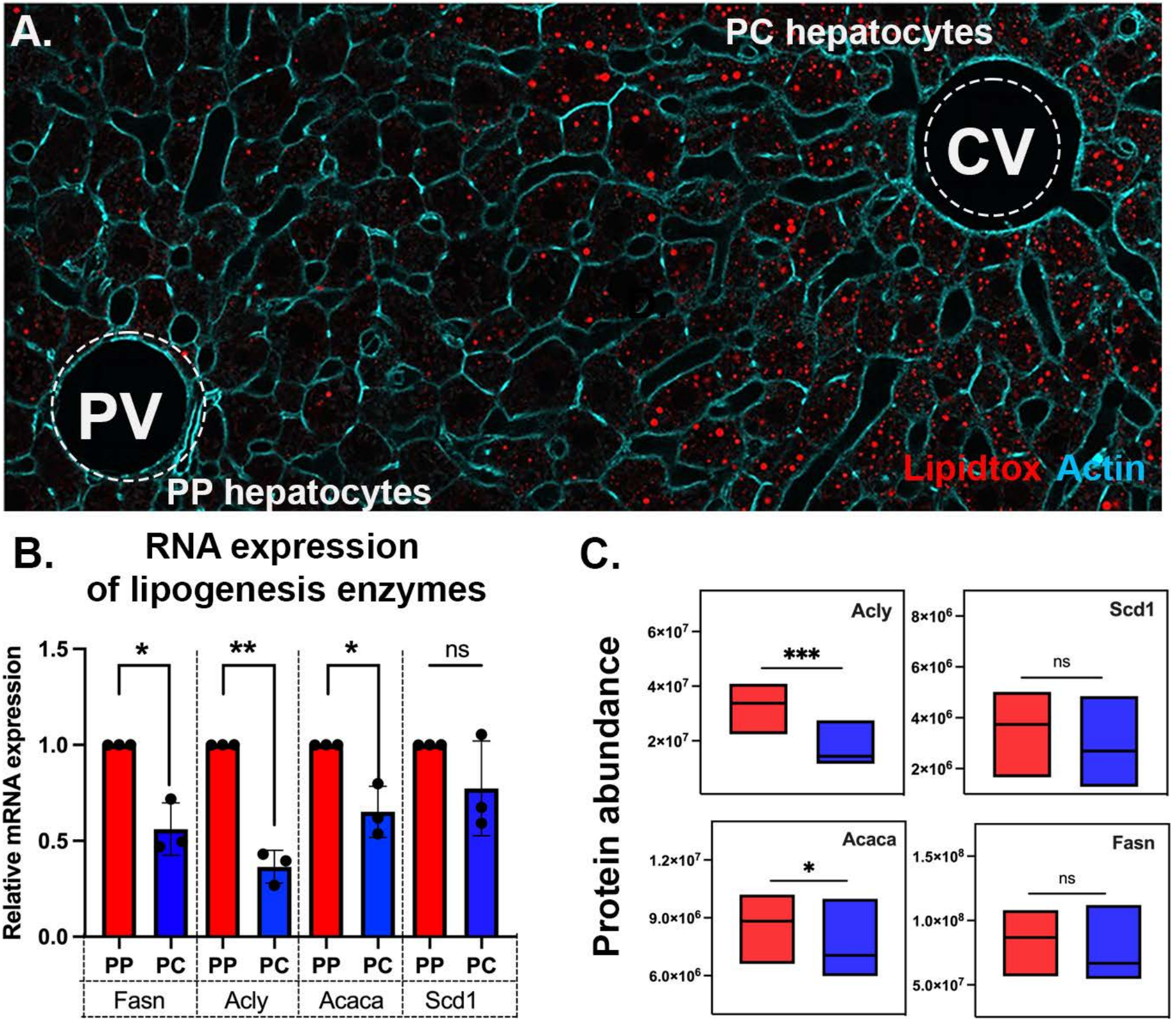

Fig S2. Lipid synthesis is pericentral in the murine liver

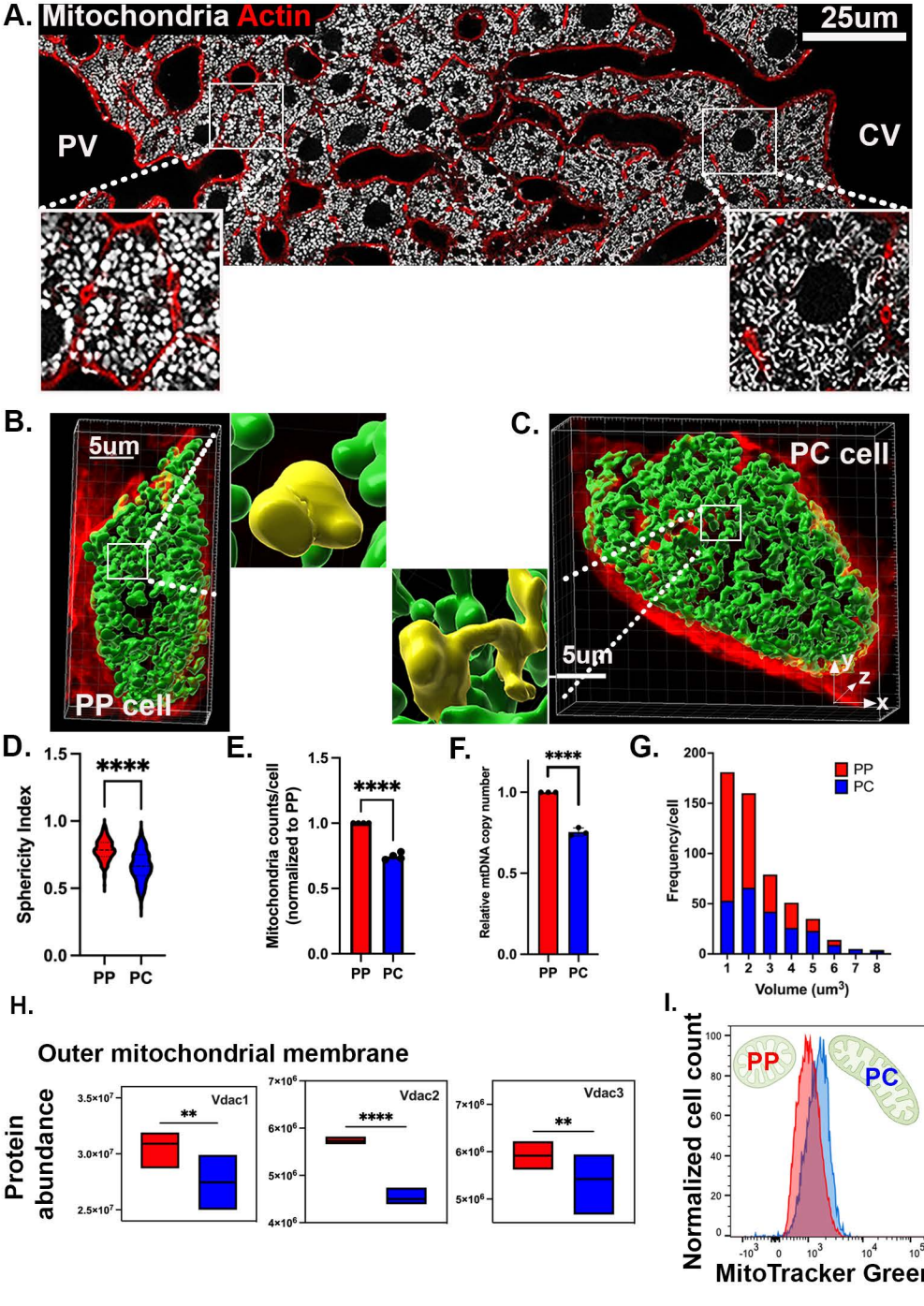

Fig 4. Mitochondrial morphology and organization across the lobule

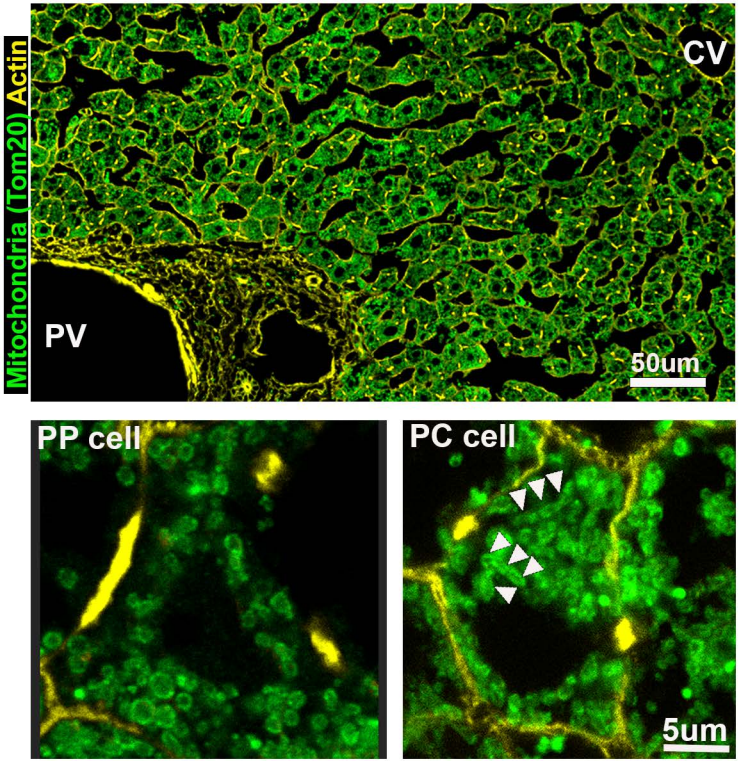

Fig S3. Mitochondrial morphologies are conserved in the human liver

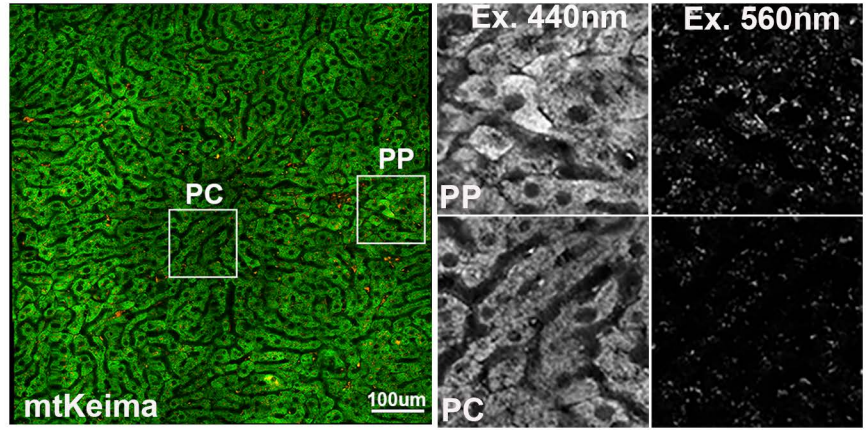

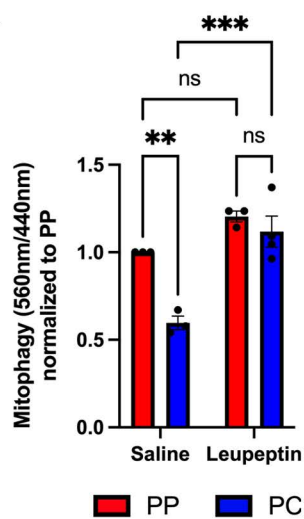

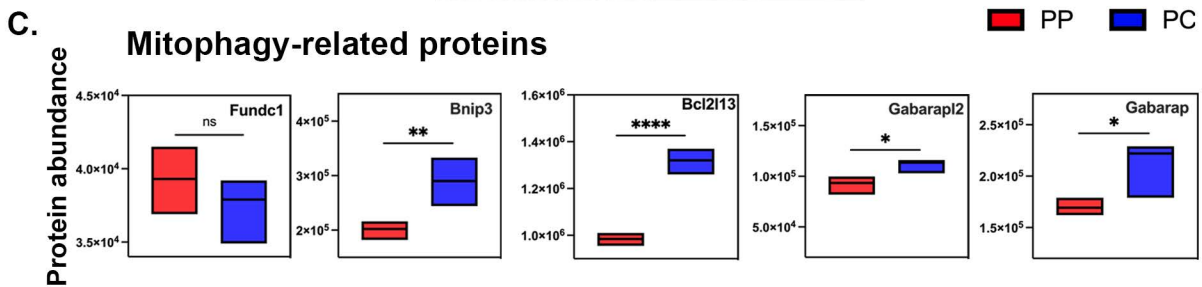

Fig 5. PP mitochondria display higher turnover via mitophagy

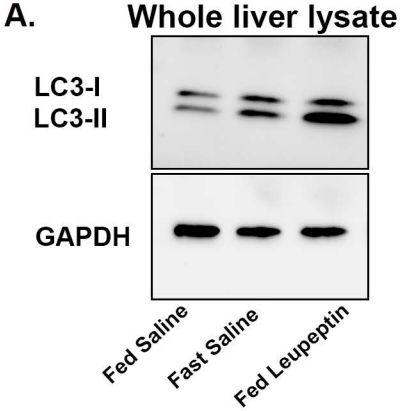

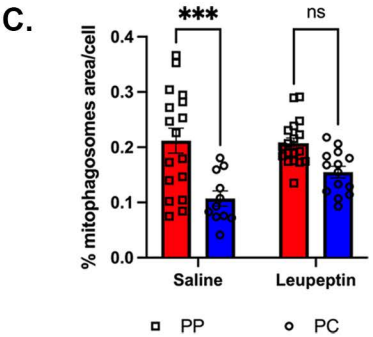

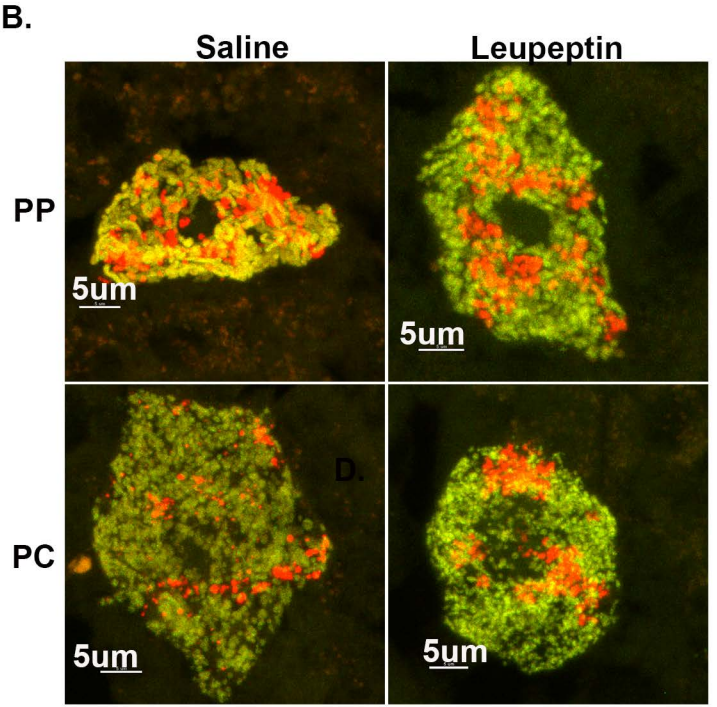

Fig S4. PP mitochondria display higher turnover via mitophagy

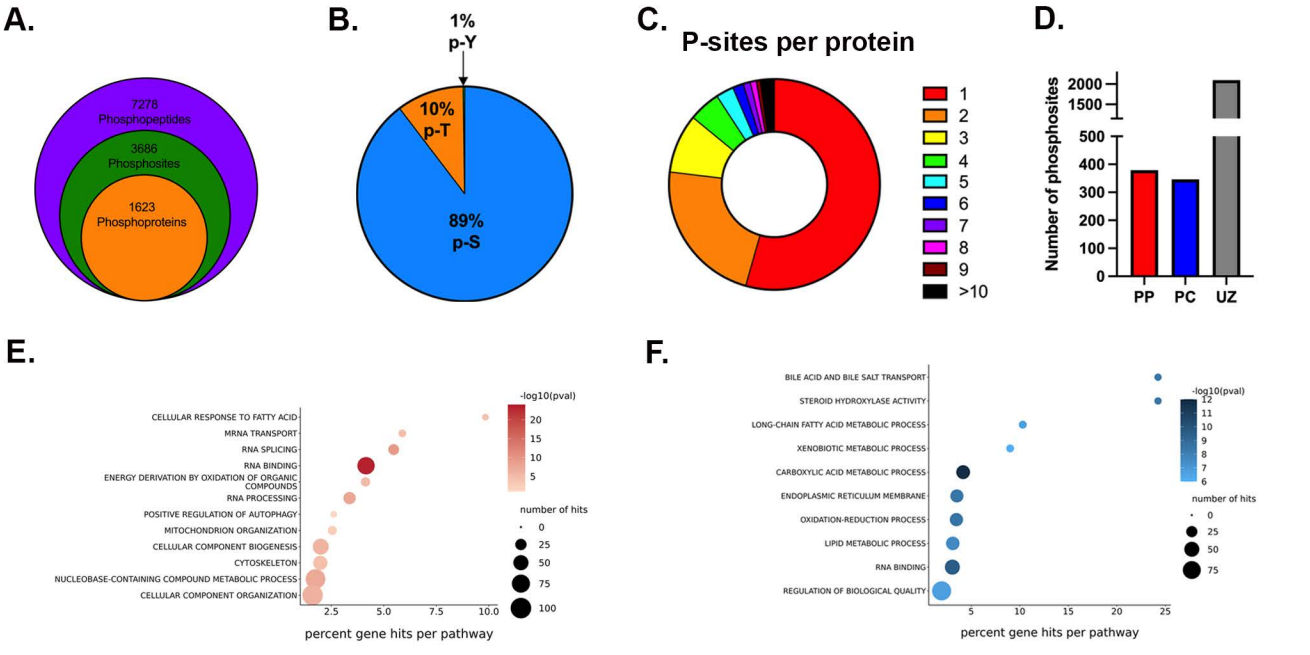

H.

Protein	Zonation	P-site	Function
Bnip3	PP	S78, S85, S88, T66	Mitophagy
Mtfr1	PP	S234/S235	Fission
Bcl2l13	PP	S387	Mitophagy
Mtfr1l	PP	T118	Fission
Prkaca	PP	T198	cAMP-PKA signaling
Apex1	PP	S18	mtDNA maintenance
Slirp	PP	S105	mtRNA stability
Rmdn3	PP	S46, S50	Mitochondrial dynamics/contact sites
Tfam	PP	S241	mtDNA maintenance
Tomm70	PP	S94	Protein import and sorting
Ehhadh	PP	T543	Fatty acid oxidation
Mrps36	PC	S55/T59/S60	Mitochondrial translation
Bckdk	PC	S31	Amino acid metabolism
Pdha1	PC	S293, S300	Pyruvate metabolism
Miga2	PC	S276	Fusion/contact sites
Gpam	PC	S694	phospholipid metabolism
Nags	PC	S44	Amino acid metabolism
Coq9	PC	S81	Coenzyme Q metabolism
Hsd17b8	PC	S58	Lipid biosynthesis
Akap1	PC	T487	cAMP-PKA signaling

Fig 6. Phosphoproteome highlights spatially regulated pathways contributing to mitochondrial phenotypes

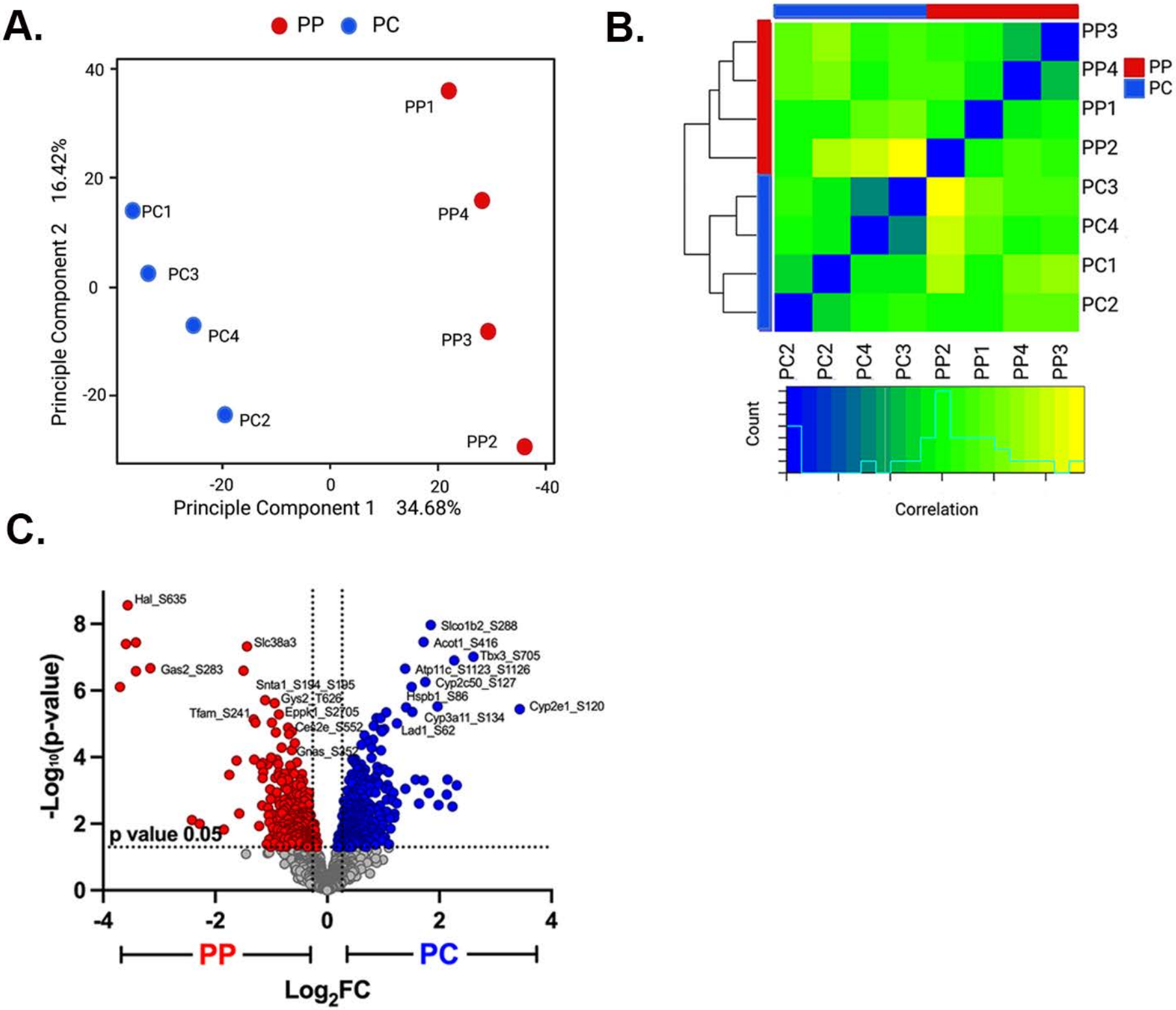

Fig S5 Hepatocyte phosphoproteome

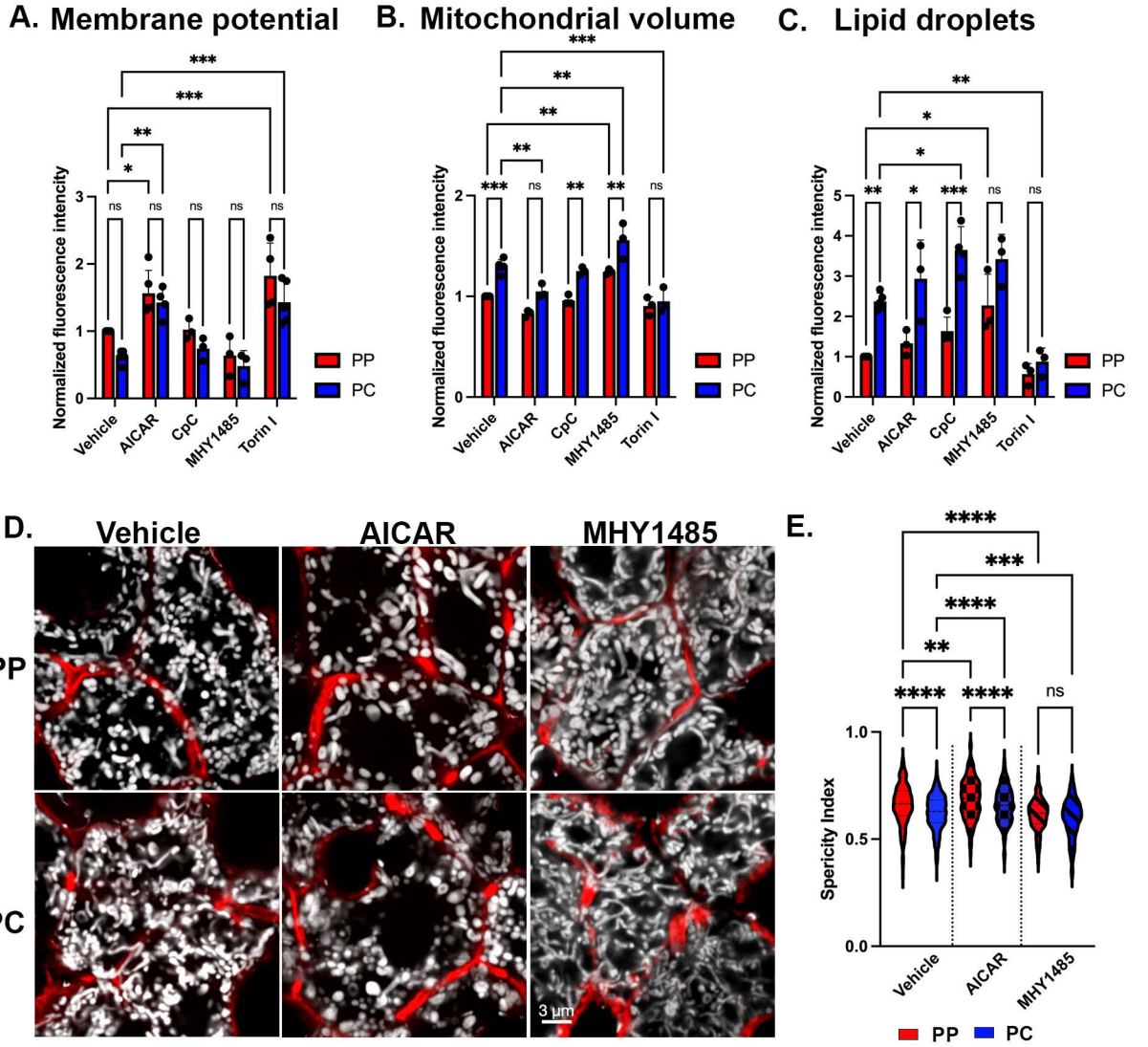

Fig 7. Nutrient sensing signaling regulate mitochondrial functional and morphological diversity

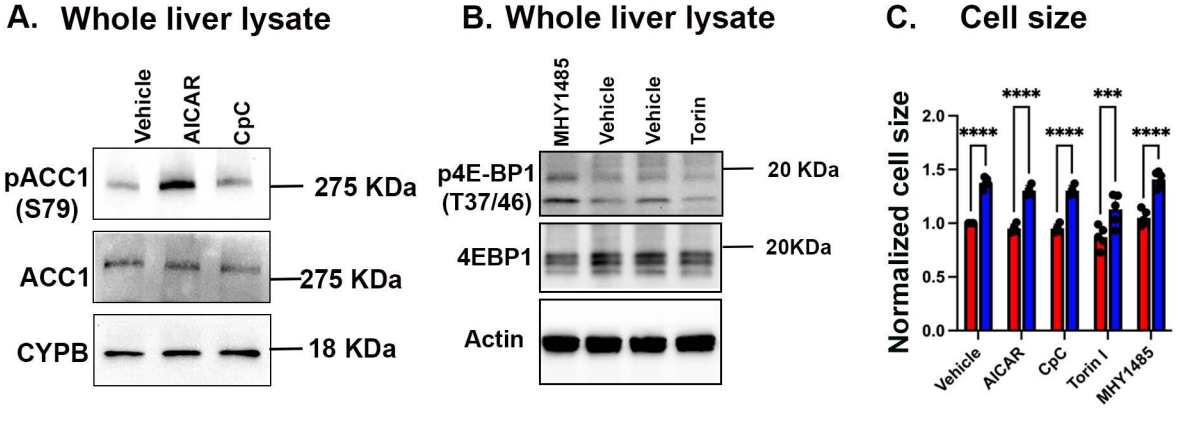

Fig S6. Nutrient sensing signaling regulates mitochondrial heterogeniety